



## An Optimized Hybrid Modulation Scheme for Reducing Conduction Losses in Dual Active Bridge Converters

Liu, Bochen; Davari, Pooya; Blaabjerg, Frede

*Published in:*

I E E E Journal of Emerging and Selected Topics in Power Electronics

*DOI (link to publication from Publisher):*

[10.1109/JESTPE.2019.2956323](https://doi.org/10.1109/JESTPE.2019.2956323)

*Publication date:*

2021

*Document Version*

Accepted author manuscript, peer reviewed version

[Link to publication from Aalborg University](#)

*Citation for published version (APA):*

Liu, B., Davari, P., & Blaabjerg, F. (2021). An Optimized Hybrid Modulation Scheme for Reducing Conduction Losses in Dual Active Bridge Converters. *I E E E Journal of Emerging and Selected Topics in Power Electronics*, 9(1), 921-936. Article 8915697. <https://doi.org/10.1109/JESTPE.2019.2956323>

### General rights

Copyright and moral rights for the publications made accessible in the public portal are retained by the authors and/or other copyright owners and it is a condition of accessing publications that users recognise and abide by the legal requirements associated with these rights.

- Users may download and print one copy of any publication from the public portal for the purpose of private study or research.
- You may not further distribute the material or use it for any profit-making activity or commercial gain
- You may freely distribute the URL identifying the publication in the public portal -

### Take down policy

If you believe that this document breaches copyright please contact us at [vbn@aub.aau.dk](mailto:vbn@aub.aau.dk) providing details, and we will remove access to the work immediately and investigate your claim.

# An Optimized Hybrid Modulation Scheme for Reducing Conduction Losses in Dual Active Bridge Converters

Bochen Liu, *Student Member, IEEE*, Pooya Davari, *Senior Member, IEEE*, Frede Blaabjerg, *Fellow, IEEE*

**Abstract**—A linearized hybrid modulation scheme for the DAB converter is proposed in this paper. For the purpose of minimizing the conduction losses dissipated on the transformer and the power transistors, an optimal relationship function between the two control variables employed in extended phase shift (EPS) modulation can be derived. However, the obtained relationship function is a complex expression, which is not good for simple on-line control. Hence, a linearized modulation scheme is proposed in this paper. This modulation scheme can achieve a quasi-minimum RMS value of the leakage inductance current for the same output power. Meanwhile, the zero voltage switching (ZVS) of the power transistors can be achieved over the whole power range. The power transfer capability is also kept same as the optimal EPS scheme. Finally, experiments are conducted on a laboratory prototype to validate the effect of the linearized modulation scheme on the reduction of conduction losses. The experimental results present an improved converter efficiency and the realization of ZVS.

## I. INTRODUCTION

Firstly proposed in 1988 [1], the dual active bridge (DAB) converter is now widely used in many applications such as distributed power systems and energy storage [2], [3]. Due to its advantages of galvanic isolation and bidirectional power flow, DAB converters are applied among multiple dc energy sources such as battery packs, ultra-capacitors and photovoltaic submodules to match various voltage levels [4]–[7]. Moreover, since the DAB converter can naturally achieve zero voltage switching (ZVS) without any auxiliary components and has a simple and symmetrical structure, it is also a potential candidate for high efficiency and high power density applications such as electric vehicles and aerospace [8]–[11]. For the same reason, the DAB is also an ideal dc-dc conversion choice for applications where modular design is often needed such as energy storage systems and power electronic transformers.

A conventional way to control the DAB converter is using single phase shift (SPS) modulation to fulfill the power/voltage/current requirements. SPS is simple and easy for real time control. However, utilizing this simple modulation scheme can not guarantee ZVS if the voltage ratio deviates far from one, which results in poor efficiency at partial load conditions. Notably, under this situation, even the switches might be broken with excessive  $dv/dt$  caused by ZVS failure

[12]–[14]. In order to overcome this drawback, many improved modulation methods are introduced to extend the DAB soft-switching operating range, such as extended phase-shift (EPS) modulation [15], dual phase-shift (DPS) modulation [16], [17] and triple phase-shift (TPS) modulation [18]–[21]. Other than only one phase shift in SPS, these improved modulation schemes try to introduce more control variables.

In the simple SPS modulation, only the outer phase shift between the primary and the secondary full bridge is regulated, leading to a two-level primary and secondary winding voltage. If varying inner phase shift (as defined in Section II-B) is considered, the winding voltages turn to three-level because the diagonal switches in each full bridge are not turned on or off synchronously any more. Taking [21] as an example, a comprehensive searching of operation modes with TPS is implemented, and the corresponding soft-switching boundaries for each operation mode are derived. However, the analysis of power transfer range is absent, which is important for selecting proper operation mode due to the varying given powers.

Alternatively, applying multiple control variables makes it possible to realize a more ambitious target, such as current stress optimization [22]–[26], backflow power reduction [27] and non-active power loss minimization [28]. Actually, these optimization targets are based on optimizing different parts of the leakage inductance current, e.g. current stress optimization usually refers to reducing the peak value of the leakage inductance current, backflow power is often related to the intervals when the current direction is reversed into the power source.

Besides, many optimized control schemes are focusing on reducing the root mean square (RMS) value of the leakage inductance current [29]–[32], which is closely related to the conduction losses of the power semiconductors and high-frequency transformer. Notably, hybrid modulation methods could be adopted in order to extend the converter performance over a wide operation range [33], [34]. Furthermore, the switching frequency can also be varied aiming at specific optimization objects. In [35], the switching frequency is varied to modulate the DAB in a specific single-stage ac-dc converter. In [36], the circulating current is minimized over a wide power range using variable frequency modulation.

Among the aforementioned modulation methods, some of them are complicated and not easy to implement. One usual situation is that in order to make the DAB converter work at the optimal operation point, massive calculations are often conducted to handle those complex relationships among the

This paper is an extension of the conference paper with the title of “An Optimized Control Scheme for Reducing Conduction and Switching Losses in Dual Active Bridge Converters”, which was presented in Proc. IEEE Energy Conversion Congress and Exposition (ECCE), 2018.

control variables. The reason is that at least three limitations should be taken into account during the operation, i.e. the ZVS range, the power transfer capability and the optimization targets. Of course, there exist other factors depending on different requirements, such as the voltage variation range, the transient response or the effect of the passive components. One way to solve the complexity is to adopt a look-up table in the control process, where the optimal operation points are calculated in advance and input into a table prior to the converter operation. But the performance of this method is adversely affected by the components mismatched parameters due to their tolerances, temperature dependency and lifetime. Moreover, a large memory is needed to guarantee the accuracy if the converter has to work in a wide operation range. In terms of the variable switching frequency modulation, one large challenge is the design of passive components and the electromagnetic interference filter.

In order to make the DAB converter more adaptive and applicable, this paper proposes an optimized hybrid modulation scheme to simplify the control process based on EPS modulation. The main contributions of this paper are:

- The comprehensive analysis of the power transfer range for each operation mode, which is derived based on the ZVS conditions rather than operation mode boundary conditions as in some literature.
- The analytical optimization expressions for each operation mode are derived in order to minimize the RMS value of the leakage inductance current.
- Several simplified optimization methods are proposed based on different voltage ratio requirements and preferred working conditions in various applications.
- Independent of the voltage ratio limitation and being simpler than other methods, the linearized optimization method is applied to the available DAB setup in this paper and validated by the experimental results.

This paper is organized as follows. Firstly, the EPS based operation modes for boost and buck scenarios under ZVS conditions are presented in Section II. Next, according to the derived operation modes in Section II and selected components for the DAB setup, the losses distribution are calculated in Section III. In Section IV, an optimal modulation scheme (called ‘OMS1’ in the following) is firstly derived. In order to simplify this scheme and considering different voltage ratio requirements, three approximated modulation schemes are developed. With the aim of selecting the most suitable modulation method, a through comparison is presented among these four schemes at the end of Section IV. Therefore, in Section V, the selected linear scheme is applied into a laboratory prototype to validate the feasibility on conduction losses reduction and ZVS realization. Finally, conclusions are given in Section VI.

## II. BASIC MODULATION METHODS FOR DUAL ACTIVE BRIDGE CONVERTERS

### A. DAB Model

The topology of the DAB converter is shown in Fig. 1. It consists mainly of two full bridges  $HB_1$  and  $HB_2$ , the

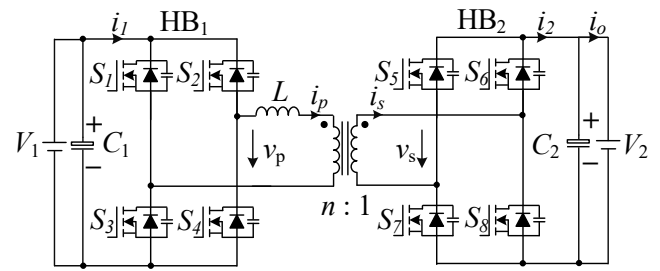


Fig. 1. Topology of the dual active bridge (DAB) converter.

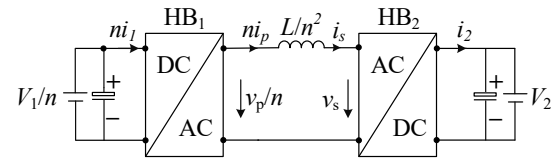


Fig. 2. Simplified DAB model by referring the converter to the secondary side of the transformer.

middle terminals of which are linked by a high-frequency transformer and the side ends are paralleled with the input and output dc voltage ports. In order to flexibly adjust the leakage inductance, an auxiliary inductor is cascaded with the high-voltage primary winding so that a lower additional power loss is induced compared to the secondary low-voltage high-current winding.

The magnetizing inductance is considered much larger than the leakage inductance, leading to negligible magnetizing current compared with the load current. Therefore in the T-type transformer equivalent circuit, the branch with magnetizing inductor can be seen as an open circuit. On this basis, the DAB model is obtained as shown in Fig. 2 after referring the circuit parameters to the secondary side.

### B. Operation Modes

Due to the bidirectional power transfer ability and the symmetrical topology, the DAB converter has four operating scenarios: forward/backward, buck/boost. Assuming the power flow is from the primary side to the secondary side, a factor  $k$  is introduced as

$$k = \frac{V_1}{nV_2} \quad (1)$$

to signify the voltage ratio.  $k < 1$  and  $k > 1$  denote boost and buck scenarios, respectively.

In order to simplify the calculations, the base power  $P_b$  and base current  $I_b$  defined in (2) are used to normalize the real values. Therein,  $V_1$ ,  $V_2$  and  $f_{sw}$  denote the input, output dc voltage and the switching frequency, respectively.  $L$  is the total inductance consisting of the transformer leakage inductance and the auxiliary inductance.

$$P_b = \frac{(nV_2)^2}{8Lf_{sw}}, \quad I_b = \frac{n^2V_2}{8Lf_{sw}} \quad (2)$$

The power is mainly controlled by the outer phase shift  $\varphi$ , which is the displacement angle between the fundamental components of  $v_p$  and  $v_s$ . If  $D_\varphi = \varphi/\pi$  is defined for

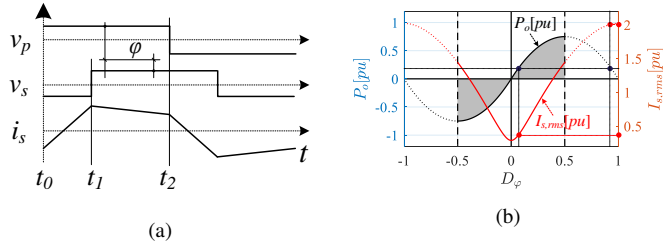


Fig. 3. (a) typical SPS working waveforms over one switching period, which is a special case of EPS by setting  $D_\alpha = 1$  in Mode II (b) the output power  $P_o$  and the RMS leakage inductance current  $I_{L,rms}$  of the DAB converter with respect to  $D_\varphi$ ,  $k = 0.75$  in this case.

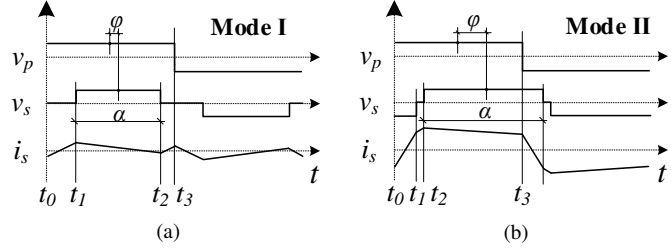


Fig. 4. In boost scenario, typical EPS working waveforms in one switching period (a) Mode I,  $D_\varphi < (1 - D_\alpha)/2$  (b) Mode II,  $D_\varphi > (1 - D_\alpha)/2$ .

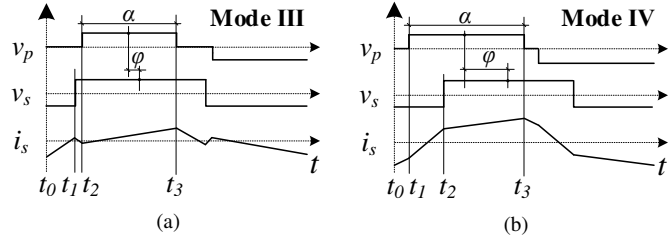


Fig. 5. In buck scenario, typical EPS working waveforms in one switching period (a) Mode III,  $D_\varphi < (1 - D_\alpha)/2$  (b) Mode IV,  $D_\varphi > (1 - D_\alpha)/2$ .

simplification,  $D_\varphi \in [0, 1]$  stands for forward power flow from  $V_1$  to  $V_2$  and  $D_\varphi \in [-1, 0]$  for the reverse direction. In fact,  $D_\varphi$  is often limited in  $[-0.5, 0.5]$  to lower the RMS value of the leakage inductance current while maintaining the same power transfer capability, which can be explained by Fig. 3.

Given the SPS working waveforms in Fig. 3(a) and with  $T_{sw} = 1/f_{sw}$ , the normalized average output power  $P_o[pu] = 1/P_b \cdot 1/T_{sw} \cdot \int_0^{T_{sw}} [v_s(t) \cdot i_s(t)] dt$  and the normalized RMS leakage inductance current  $I_{s,rms}[pu] = 1/I_b \cdot \sqrt{1/T_{sw} \cdot \int_0^{T_{sw}} i_s^2(t) dt}$  are derived as

$$P_o[pu] = 4kD_\varphi(1 - D_\varphi) \quad (3)$$

$$I_{s,rms}[pu] = \frac{2\sqrt{3}}{3} \cdot \sqrt{(12D_\varphi^2 - 8D_\varphi^3 - 2)k + k^2 + 1} \quad (4)$$

which can be represented by the black curve and red curve in Fig. 3(b), respectively. It can be seen that there are always two points in the ranges of  $[0, 0.5]$  and  $[0.5, 1]$  for the same power, but the leakage inductance current is smaller in  $[0, 0.5]$ . This conclusion is also applicable to other phase-shift modulation schemes including EPS.

In EPS, considering the voltage-second balance of the leakage inductor, two operation modes can be found for boost

TABLE I

EXPRESSIONS OF THE NORMALIZED LEAKAGE INDUCTANCE CURRENT DURING DIFFERENT INTERVALS FOR EACH EPS OPERATION MODE

| Mode I --> Fig. 4(a)   |  |
|------------------------|--|
| $[t_0, t_1]$           | $i_s(t)[pu] = \frac{8k}{T_{sw}}t - 2k + 2D_\alpha$                           |
| $[t_1, t_2]$           | $i_s(t)[pu] = \frac{8(k-1)}{T_{sw}}t + 2 - 2k + 4D_\varphi$                  |
| $[t_2, t_3]$           | $i_s(t)[pu] = \frac{8k}{T_{sw}}t - 2k - 2D_\alpha$                           |
| Mode II --> Fig. 4(b)  |  |
| $[t_0, t_1]$           | $i_s(t)[pu] = \frac{8(k+1)}{T_{sw}}t - 2k - 4D_\varphi + 2$                  |
| $[t_1, t_2]$           | $i_s(t)[pu] = \frac{8k}{T_{sw}}t - 2k + 2D_\alpha$                           |
| $[t_2, t_3]$           | $i_s(t)[pu] = \frac{8(k-1)}{T_{sw}}t - 2k + 2 + 4D_\varphi$                  |
| Mode III --> Fig. 5(a) |  |
| $[t_0, t_1]$           | $i_s(t)[pu] = \frac{8}{T_{sw}}t - (2k-2)D_\alpha - 4D_\varphi$               |
| $[t_1, t_2]$           | $i_s(t)[pu] = -\frac{8}{T_{sw}}t - (2k+2)D_\alpha + 4D_\varphi + 4$          |
| $[t_2, t_3]$           | $i_s(t)[pu] = \frac{8(k-1)}{T_{sw}}t + (2k-2)D_\alpha + 4D_\varphi + 4 - 4k$ |
| Mode IV --> Fig. 5(b)  |  |
| $[t_0, t_1]$           | $i_s(t)[pu] = \frac{8}{T_{sw}}t - (2k-2)D_\alpha - 4D_\varphi$               |
| $[t_1, t_2]$           | $i_s(t)[pu] = \frac{8(k+1)}{T_{sw}}t + (2k+2)D_\alpha - 4D_\varphi - 4k$     |
| $[t_2, t_3]$           | $i_s(t)[pu] = \frac{8(k-1)}{T_{sw}}t + (2k-2)D_\alpha + 4D_\varphi + 4 - 4k$ |

TABLE II

COMBINED LIMITATIONS BY ZVS AND OPERATIONAL CONSTRAINTS

|          |   |
|----------|---|
| Mode I   | $2k/(1-k)D_\varphi < D_\alpha < k, \quad 0 < D_\varphi < (1-k)/2$     |
| Mode II  | $D_\alpha > 2k(1-D_\varphi)/(1+k), \quad (1-k)/2 < D_\varphi < 1/2$   |
| Mode III | $2D_\varphi/(k-1) < D_\alpha < 1/k, \quad 0 < D_\varphi < (k-1)/(2k)$ |
| Mode IV  | $D_\alpha > 2(1-D_\varphi)/(1+k), \quad (k-1)/(2k) < D_\varphi < 1/2$ |

or buck scenario, as shown in Fig. 4 and Fig. 5, respectively. If the inner phase shift is denoted by  $D_\alpha = \alpha/\pi$ , then  $\alpha \in [0, \pi]$  corresponds to  $D_\alpha \in [0, 1]$ . Clearly, if  $D_\alpha = 1$ , EPS is fallen into SPS. In this regard, SPS can be seen as a special case of EPS.

The current waveform is shaped by the voltage drop on the leakage inductor.

$$\frac{L}{n^2} \frac{di_s(t)}{dt} = \frac{v_p(t)}{n} - v_s(t) \quad (5)$$

Considering  $i_s(t_0) = i_s(t_3)$  in half switching period ( $t_3 = T_{sw}/2$ ), the segmented current can be calculated, as listed in Table I.

In order to achieve zero-voltage switching for all switches, the parasitic capacitor of each off-state transistor should be fully discharged at first, which happens through the resonance of the parasitic capacitor  $C_{oss}$  and the leakage inductance

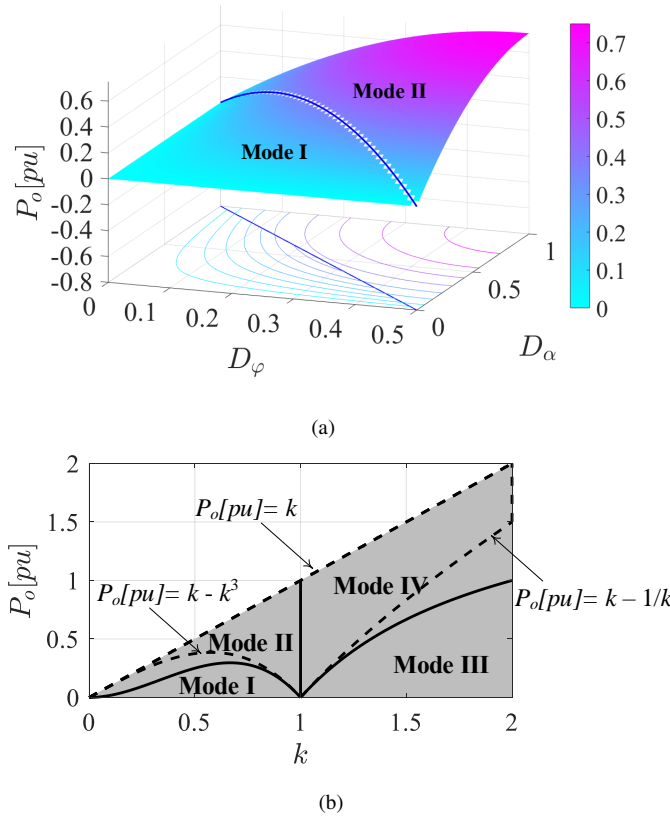


Fig. 6. (a) Output power in terms of  $D_\alpha$  and  $D_\phi$  with the blue curve as the operational constraint. (b) ZVS-limited power transfer range in terms of  $k$ : gray area is the ZVS range for EPS and it is divided into 4 parts (i.e. 4 modes) by solid curves. The area encircled by dashed lines is ZVS range for SPS.

*L.* Afterwards, the body diode will be naturally conducted, resulting in a near-zero source-to-drain voltage  $V_{DS}$  (the actual value is equal to the voltage drop on the body diode). Thus zero-voltage switching can be achieved if the transistor is turned on at this moment, indicating that the direction of the current flow is from source to drain at the switching-on instants for  $S_1 \sim S_8$ . According to this constraint, the polarity of the leakage current at switching instants can be confirmed and the ZVS conditions can be further derived with the current expressions in Table I. Then associating with the operational constraints for each mode, the combined limitations on the control variables are attained in Table II.

### C. ZVS-limited Power Transfer Range

Using the current expressions in Table I, the average output power in one switching period can be calculated with

$$P_o[pu] = \begin{cases} 4kD_\alpha D_\phi & \text{Mode I,III} \\ -k[4D_\phi^2 - 4D_\phi + (1 - D_\alpha)^2] & \text{Mode II,IV} \end{cases} \quad (6)$$

Since  $D_\phi$  in I, III is smaller, the power transmission ability is weaker compared to II, IV, as shown in Fig. 6(a). In other words, Mode I and Mode III are suitable for lower power transmission while Mode II and Mode IV for higher. On this

basis, the limited power transfer range by considering the ZVS constraints in Table II can be derived as

$$P_o[pu] \in \begin{cases} \left\{ \begin{array}{l} (0, 2k^2(1-k)] \rightarrow \text{Mode I} \\ (2k^2(1-k), k] \rightarrow \text{Mode II} \end{array} \right\} k < 1 \\ \left\{ \begin{array}{l} (0, 2(k-1)/k] \rightarrow \text{Mode III} \\ (2(k-1)/k, k] \rightarrow \text{Mode IV} \end{array} \right\} k > 1 \end{cases} \quad (7)$$

and shown by the gray area in Fig. 6(b). For comparison, in SPS, due to the ZVS conditions  $D_\phi > (1-k)/2$  and  $D_\phi > (k-1)/(2k)$ , the power range limited by

$$P_o[pu] \in \begin{cases} [k - k^3, k] \rightarrow k < 1 \\ [k - 1/k, k] \rightarrow k > 1 \end{cases} \quad (8)$$

is also plotted in Fig. 6(b). The boundary conditions in (8) are denoted by the dashed lines in Fig. 6(b). Varying with the voltage ratio  $k$ , the ZVS can be theoretically achieved from zero to the maximum power in EPS, while this is applicable to SPS only when  $k = 1$ . In other words, the ZVS range is considerably extended in EPS because of the introduced control variable  $D_\alpha$ .

## III. LOSSES DISTRIBUTION

### A. Transformer and Auxiliary Inductor

The losses of the magnehtical components include copper losses and core losses. For the given transformer and inductor in Table III, the copper losses can be calculated with

$$P_{cond,Tr} = \left( \frac{R_L + R_{Trp}}{n^2} + R_{Trs} \right) \cdot I_{s,rms}^2 \quad (9)$$

where  $R_L$  is the auxiliary inductor resistance, and  $R_{Trp}$ ,  $R_{Trs}$  are the primary and secondary winding resistances of the transformer, respectively.

For simplification, assuming the transformer and inductor are fed by the fundamental sinusoidal components, this allows for calculating core losses with the Steinmetz equation [39]

$$p_v = C_m f_{sw}^\alpha \hat{B}^\beta \quad (10)$$

and the core volume  $V_{Tr}$  and  $V_L$ , respectively. The peak magnetic flux density  $\hat{B}$  is estimated with  $\hat{B}_{Tr} \approx 2V_1/(\pi^2 f_{sw} N_{Trp} A_{Tr})$  ( $N_{Trp}$ : primary winding turns,  $A_{Tr}$ : effective magnetic cross section) and  $\hat{B}_L \approx \mu_{eff} \mu_0 N_L \hat{I}_L / l_L$  ( $\mu_{eff}$ : equivalent relative permeability of a gapped core,  $N_L$ : winding turns,  $\hat{I}_L$ : peak inductor current,  $l_L$ : effective magnetic path length) for the transformer and auxiliary inductor, respectively. Detailed information is listed in Table IV.

### B. Power Switches

The losses caused by the power semiconductors mainly consist of conduction and switching losses. For the calculation of the conduction losses, the RMS switch currents can be easily derived from the RMS transformer current  $I_{s,rms}$  due to that every switch conducts current during half of the switching period. Therefore, given the switch parameters in Table III, the conduction losses of the power switches can be calculated with

$$P_{cond,sw} = 4 \cdot \frac{R_{DSonp}}{N_{swp}} \cdot \left( \frac{I_{s,rms}}{\sqrt{2}n} \right)^2 + 4 \cdot \frac{R_{DSons}}{N_{sws}} \cdot \left( \frac{I_{s,rms}}{\sqrt{2}} \right)^2 \quad (11)$$

TABLE III  
COMPONENTS PARAMETERS OF THE IMPLEMENTED PROTOTYPE

| Components  | Parameters   |
|---|--|
| Primary winding of the DAB HF transformer: 35 turns copper foil   | $R_{Trp}=607.9 \text{ m}\Omega$<br>@ $T_a=25 \text{ }^\circ\text{C}$ |
| Secondary winding of the DAB HF transformer: 10 turns copper foil | $R_{Trs}=16.5 \text{ m}\Omega$<br>@ $T_a=25 \text{ }^\circ\text{C}$  |
| Auxiliary inductor:<br>10 turns Litz wire, 20 strands, 0.355 mm   | $R_L=27.9 \text{ m}\Omega$<br>@ $T_a=25 \text{ }^\circ\text{C}$      |
| MOSFETs $S_1 \sim S_4$ :<br>IPW65R080CFD                          | $R_{DSonp}=72 \text{ m}\Omega$<br>@ $T_j=25 \text{ }^\circ\text{C}$  |
| MOSFETs $S_5 \sim S_8$ :<br>2 x IPP110N20N3 in parallel           | $R_{DSons}=9.6 \text{ m}\Omega$<br>@ $T_j=25 \text{ }^\circ\text{C}$ |

TABLE IV  
MAGNETIC CORE PARAMETERS

| Transformer (core type: ETD59/31/22 material: N97)        |                   |             |       |          |         |
|---|-------------------|-------------|-------|----------|---------|
| $V_{Tr}$  | $A_{Tr}$          | $N_{Trp}$   | $C_m$ | $\alpha$ | $\beta$ |
| 51.2 $\text{cm}^2$  | 368 $\text{mm}^2$ | 35          | 8.21  | 1.28     | 2.2     |
| Auxiliary Inductor (core type: ETD44/22/15 material: N87) |                   |             |       |          |         |
| $V_L$   | $l_L$             | $\mu_{eff}$ | $C_m$ | $\alpha$ | $\beta$ |
| 17.8 $\text{cm}^2$  | 10.3 $\text{cm}$  | 120         | 10    | 1.26     | 2.15    |

$R_{DSonp}/N_{swp}$  and  $R_{DSons}/N_{sws}$  are the equivalent switch on-state resistance if each switch consists of  $N_{swp}$  and  $N_{sws}$  paralleled semiconductors in the primary and secondary full-bridges, respectively.

On the basis of ZVS turn-on, only turn-off losses are considered for calculating switching losses for each transistor, which can be estimated by [40]

$$p_{sw} = U_{DS} \cdot I_{off} \cdot \frac{t_{ru} + t_{fi}}{2} \cdot f_{sw} \quad (12)$$

where  $U_{DS}$  denotes the turn-off voltage and  $I_{off}$  is the current at switching-off instants.  $t_{ru}$  and  $t_{fi}$  are the voltage rise time and current fall time during switching-off transients.

### C. Capacitors

The losses dissipated on the input and output capacitors are calculated with the equivalent series resistance (ESR), which can be obtained from the datasheet, leading to

$$p_{cap} = \frac{R_{ESR}}{N_{cap}} I_c^2 \quad (13)$$

where  $N_{cap}$  is the number of parallel capacitors. The selected capacitors are one B43544A6397M000 ( $C_1=0.39 \text{ mF}$ ) on the input side and five EETEE2D301HJ in parallel ( $C_2=1.5 \text{ mF}$ ) on the output side.

### D. Losses Distribution

The total losses are the sum of all discussed power losses and can be categorized as switching losses  $P_{sw}$ , conduction losses  $P_{cond}$ , core losses  $P_{core}$  and capacitor losses  $P_{cap}$ , namely

$$P_{total} = P_{sw} + P_{cond} + P_{core} + P_{cap} \quad (14)$$

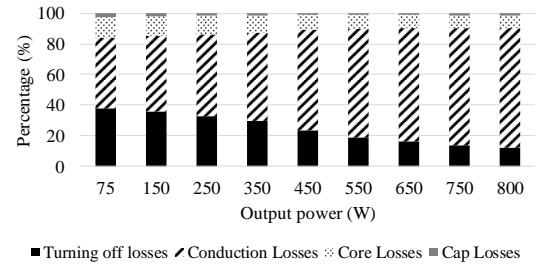


Fig. 7. Calculated losses distribution percentages.

with further specifications:

$$\begin{aligned} P_{sw} &= P_{sw,S_1 \sim S_4} + P_{sw,S_5 \sim S_8} \\ P_{cond} &= P_{cond,Tr} + P_{cond,sw} \\ P_{core} &= P_{core,Tr} + P_{core,L} \\ P_{cap} &= P_{cap,in} + P_{cap,out} \end{aligned} \quad (15)$$

Operating the converter under ZVS conditions, the calculated losses percentages of different dissipation parts are shown in Fig. 7. It can be seen that for the given setup, the conduction losses are the dominating part over the whole power range, although the switching losses are almost equal to the conduction losses in light load. Besides, the conduction losses portion increases a lot in the heavy load. therefore, reducing conduction losses is of high importance to improve the system performance.

## IV. OPTIMIZED MODULATION SCHEMES FOR REDUCING CONDUCTION LOSSES

As shown in Fig. 7, conduction losses are the major loss source for the given converter setup, which are determined by the RMS value of the leakage inductance current  $I_{s,rms}$  seen from (9) and (11). It is also shown in (6) that there are infinite combinations of  $D_\alpha$  and  $D_\varphi$  for the same average output power, which provides the possibility to reduce the conduction losses without sacrificing other performances. Fig. 8 illustrates an example of operating waveforms with different values of  $D_\alpha$  and  $D_\varphi$  but with the same output power. Clearly, the RMS current in Fig. 8(b) is smaller than Fig. 8(a).

As proved in the following, for different output power levels, there exist an optimal operating point at which the leakage inductance current is minimized and simultaneously the ZVS can be guaranteed. But the derived analytical solutions are too complex for practical control. Therefore, a linearized modulation scheme is proposed to simplify the control process.

### A. Conventional Current Minimization (OMS1)

The normalized RMS currents  $I_{s,rms}[pu]$  for each operation mode are firstly derived based on the working waveforms in Fig. 4 ~ 5, and the results are listed in Table V. In order to minimize the leakage inductance current and satisfy the output power requirements at the same time, the power expression of Mode I in (6) is rewritten as  $D_\varphi = P_o[pu]/(4kD_\alpha)$  and then

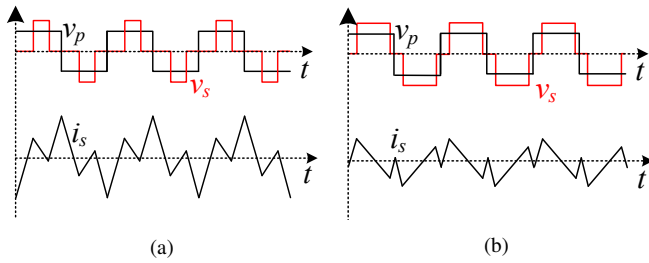


Fig. 8. Simulated working waveforms with different combinations of  $D_\alpha$  and  $D_\varphi$  (a)  $D_\alpha=0.35$ ,  $D_\varphi=0.053$  (b)  $D_\alpha=0.73$ ,  $D_\varphi=0.026$  for the same output power.

TABLE V

EXPRESSIONS OF THE NORMALIZED LEAKAGE INDUCTANCE CURRENT FOR EACH OPERATION MODE

| Operation Mode | RMS leakage inductance current $I_{s,rms}[pu]$   |
|----------------|--|
| Mode I         | $\frac{2}{3} \cdot \text{sqr}t \left[ 3(k-2)D_\alpha^3 + 9D_\alpha^2 + (36D_\varphi^2 - 9)kD_\alpha + 3k^2 \right]$  |
| Mode II        | $\frac{2}{3} \cdot \text{sqr}t \left[ -6D_\alpha^3 + (-18kD_\varphi + 9k + 9)D_\alpha^2 + (36D_\varphi - 18)kD_\alpha + 3k^2 + 3k(1-2D_\varphi)^3 \right]$   |
| Mode III       | $\frac{2}{3} \cdot \text{sqr}t \left[ 3 - (6k^2 - 3k)D_\alpha^3 + 9k^2D_\alpha^2 - 3kD_\alpha(3 - 12D_\varphi^2) \right]$                                    |
| Mode IV        | $\frac{2}{3} \cdot \text{sqr}t \left[ -6k^2D_\alpha^3 + (9k^2 - 18kD_\varphi + 9k)D_\alpha^2 - (18 - 36D_\varphi)kD_\alpha + 3 - 3(1-2D_\varphi)^3k \right]$ |

it is substituted into the expression of  $I_{s,rms}[pu]$  in Table V, resulting in

$$I_{s,rms}[pu] = \frac{2}{3} \cdot \sqrt{3(k-2)D_\alpha^3 + 9D_\alpha^2 + \left( \frac{9P_o[pu]^2}{4k^2D_\alpha^2} - 9 \right)kD_\alpha + 3k^2} \quad (16)$$

For achieving the extreme value of  $I_{s,rms}[pu]$  for a certain output power  $P_o[pu]$ , the differential of (16) with respect to  $D_\alpha$  is set to be 0, namely  $\partial I_{s,rms}[pu]/\partial D_\alpha = 0$ , solving which will lead to

$$(12k^2 - 24k)D_\alpha^4 + 24kD_\alpha^3 - 12k^2D_\alpha^2 - 3P_o[pu]^2 = 0 \quad (17)$$

It is difficult to directly solve for the analytical solution of (17) due to the high order of  $D_\alpha$ . So  $P_o[pu]$  in (17) is replaced by  $4kD_\alpha D_\varphi$ , and the simplified result is

$$(k-2)D_\alpha^2 + 2D_\alpha - k(4D_\varphi^2 + 1) = 0 \quad (18)$$

Then it becomes easy to obtain the solutions of (18), which are

$$D_{\alpha 1} = \frac{1 - \sqrt{(1-k)^2 - 4k(2-k)D_\varphi^2}}{2-k} \quad (19)$$

TABLE VI

OPTIMAL VARIABLES RELATIONSHIP WITH MINIMIZED LEAKAGE INDUCTANCE CURRENT IN EACH OPERATION MODE (OMS1)

|  |  |
|--|--|
| Mode I $\rightarrow$ Fig. 4(a)   |  |
| $D_{\alpha,opt1} = \frac{1 - \sqrt{(1-k)^2 - 4k(2-k)D_\varphi^2}}{2-k}$ ,                            | $0 < D_\varphi \leq \frac{1-k}{2}$                                     |
| Mode II $\rightarrow$ Fig. 4(b)  |  |
| $D_{\alpha,opt1} = \frac{2D_\varphi + k - 1 + \sqrt{(1-k-2D_\varphi)^2 + [k(1-2D_\varphi)]^2}}{k}$ , | $\text{for } \frac{1-k}{2} < D_\varphi < \frac{k-1+\sqrt{1-k^2}}{2k}$  |
| $D_{\alpha,opt1} = 1$ ,  | $\text{for } \frac{k-1+\sqrt{1-k^2}}{2k} \leq D_\varphi < \frac{1}{2}$ |
| Mode III $\rightarrow$ Fig. 5(a)   |  |
| $D_{\alpha,opt1} = \frac{k - \sqrt{(k-1)^2 - 4(2k-1)D_\varphi^2}}{2k-1}$ ,                           | $0 < D_\varphi \leq \frac{k-1}{2k}$                                    |
| Mode IV $\rightarrow$ Fig. 5(b)  |  |
| $D_{\alpha,opt1} = kD_\varphi - k + 1 + \sqrt{[(1-2D_\varphi)k-1]^2 + (1-2D_\varphi)^2}$ ,           | $\text{for } \frac{k-1}{2k} < D_\varphi < \frac{1-k+\sqrt{k^2-1}}{2}$  |
| $D_{\alpha,opt1} = 1$ ,  | $\text{for } \frac{1-k+\sqrt{k^2-1}}{2} \leq D_\varphi < \frac{1}{2}$  |

$$D_{\alpha 2} = \frac{1 + \sqrt{(1-k)^2 - 4k(2-k)D_\varphi^2}}{2-k} \quad (20)$$

In order to select the correct solution from (19) and (20), the derived ZVS conditions for Mode I (in Table II) are considered. Substituting  $D_\varphi < (1-k)/2$  into (19) and (20), the resulted

$$D_{\alpha 1} < k \quad (21)$$

$$D_{\alpha 2} > (2-2k+k^2)/(2-k) \geq k \quad (22)$$

indicate that  $D_{\alpha 1}$  satisfies the ZVS condition  $D_\alpha < k$  while  $D_{\alpha 2}$  does not. Therefore, the correct analytical solution of (18) should be  $D_{\alpha 1}$ . In other words, if (19) is satisfied, the leakage inductance current in Mode I for a certain output power will be located at the extreme value point. However, extreme values do not always mean the minimum values.

In order to verify whether  $D_{\alpha 1}$  is a proper solution of minimal  $I_{s,rms}$ , the relationships among  $I_{s,rms}$ - $D_\alpha$ - $D_\varphi$  (ref. Table V) are depicted in Fig. 9. As shown in Fig. 9(a), only the red-colored area is related to Mode I, limited by the operational condition  $D_\alpha < 1-2D_\varphi$ . It can be seen that for a certain output power, the black intersection points are the minimum  $I_{s,rms}[pu]$  at different power levels. Thus it can be concluded that  $D_{\alpha 1}$  is the correct solution for achieving the minimum  $I_{s,rms}$ , which is exactly the  $D_{\alpha,opt1}$  in Table VI.

Applying similar deriving process to Mode II, the resulting  $I_{s,rms}[pu]$  surface with respect to  $D_\alpha$  and  $D_\varphi$  is shown in Fig. 9(b). As for Mode III and Mode IV, the optimized results are directly given in Table VI, from which it can be seen that the analytical solution of  $D_\alpha$  is segmented depending on the operation range of  $D_\varphi$  in Mode II and Mode IV. Especially,

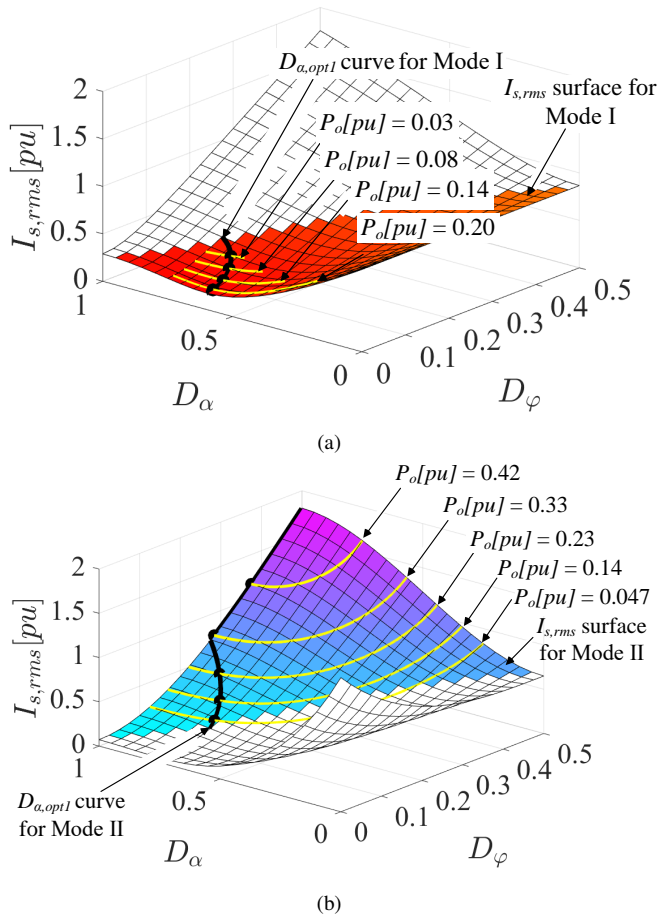


Fig. 9. 3D plot of the RMS leakage inductance current as the function of  $D_\alpha$  and  $D_\phi$  in boost scenario ( $k = 0.75$  in this case) for (a) Mode I (b) Mode II. The expressions of  $D_{\alpha,opt1}$  for achieving minimum  $I_{s,rms}$  at different power levels can be found in Table VI.

if  $D_\phi$  is close to 0.5, the optimal  $D_\alpha$  is equal to 1, meaning that the DAB converter transfers to the SPS modulation.

The modulation scheme for achieving minimum  $I_{s,rms}$  is termed as Optimized Modulation Scheme 1 (OMS1). Although the RMS leakage inductance current can be theoretically minimized by adopting  $D_{\alpha,opt1}$ , it is difficult to realize OMS1 in practical control due to the complex relationship between  $D_\alpha$  and  $D_\phi$ , as shown in Table VI.

Thus it is important to simplify the relationship expression between  $D_\alpha$  and  $D_\phi$ . Besides  $D_\alpha$  and  $D_\phi$ , the RMS leakage inductance current is also determined by the voltage ratio  $k$  (ref. Table V). For different applications, the input and output voltage may change broadly, implying various voltage ratio requirements. On this basis, the following simplifying schemes are optimized considering both conduction losses reduction and different voltage ratio ranges.

### B. Simplified Optimal Modulation Schemes

Due to the fact that the OMS1 is hard to realize, it is necessary to simplify the modulation scheme and meanwhile keep  $I_{s,rms}$  as close to the minimum value as possible for reducing the conduction losses. As shown in Fig. 10, the gray areas are limited by ZVS conditions and the colored curves denote different output powers. The derived optimal

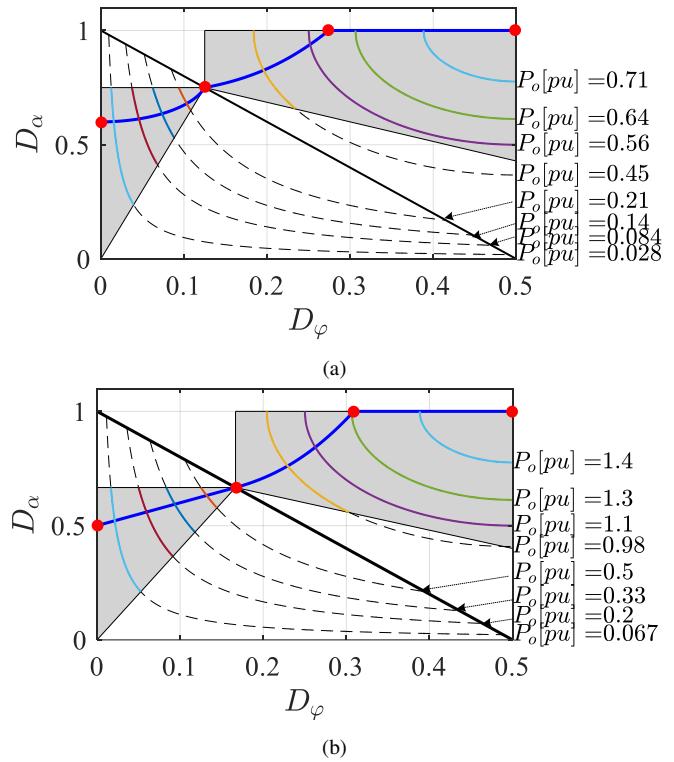


Fig. 10. The relationship function  $D_\alpha = f(D_\phi)$  in OMS1 (denoted by the blue curve) including the gray ZVS range and colored power curves in: (a) Boost scenarios ( $k = 0.75$  in this case). (b) Buck scenarios ( $k = 1.5$  in this case).

relationship  $D_\alpha = f(D_\phi)$  for minimum  $I_{s,rms}$  is represented by the blue curve. Either in buck scenario (Fig. 10(a)) or boost scenario (Fig. 10(b)), there are four key intersections induced by the segmented optimal function, which are shown by the red points. From left to right, the coordinates of these four cross points are derived as  $[0, k/(2-k)]$ ,  $[(1-k)/2, k]$ ,  $[(k-1+\sqrt{1-k^2})/(2k), 1]$ ,  $[0.5, 1]$  in Fig. 10(a), and  $[0, 1/(2k-1)]$ ,  $[(k-1)/(2k), 1/k]$ ,  $[(1-k+\sqrt{k^2-1})/2, 1]$ ,  $[0.5, 1]$  in Fig. 10(b). Since the power is increased with  $D_\phi$  and  $D_\alpha$ , three different load situations are divided by the four intersections, i.e. light load, medium load and heavy load. Based on different voltage ratio requirements and load situations, the  $D_{\alpha,opt1}$  expression can be simplified in various ways.

1) *Unified Modulation Scheme (OMS2)*: A unified modulation scheme can be derived by applying curve fitting technique among the three points  $[0, 1/(2k-1)]$ ,  $[(k-1)/(2k), 1/k]$  and  $[0.5, 1]$ , resulting in

$$D_{\alpha,opt2} = \frac{4(3k-2)}{k(k-2)}D_\phi^2 + \frac{2(2k-1)}{k}D_\phi + \frac{k}{2-k} \quad (23)$$

which is as proposed in [41]. In this scheme, only one expression is needed over the three load conditions.

Similarly, the unified modulation expression in buck scenarios also can be derived as follows.

$$D_{\alpha,opt2} = \frac{4k(2k-3)}{2k-1}D_\phi^2 + (4-2k)D_\phi + \frac{1}{2k-1} \quad (24)$$

The relation expressions denoted by (23) and (24) are plotted as the red curves in Fig. 11. Nevertheless, depending

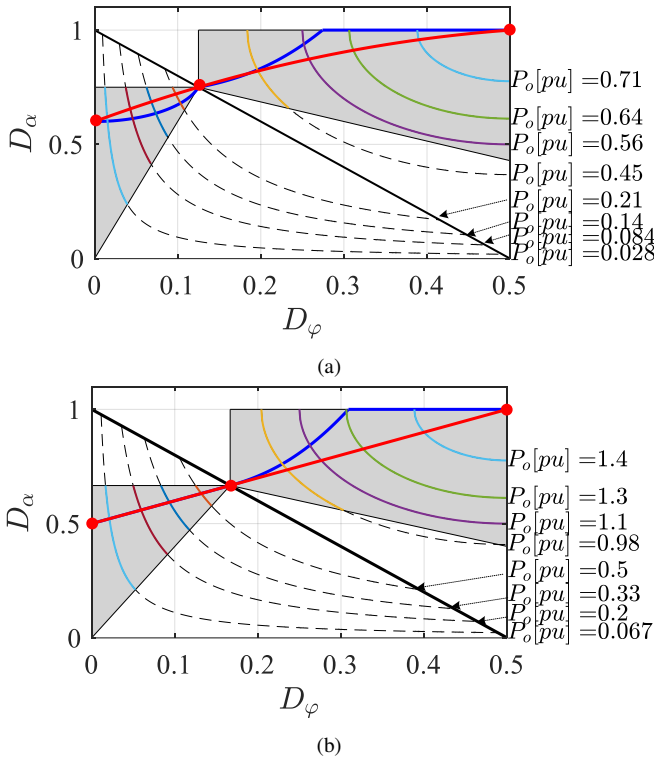


Fig. 11. The relationship function of (a) (23) for Boost scenarios ( $k = 0.75$  in this case). (b) (24) for Buck scenarios ( $k = 1.5$  in this case) in unified modulation scheme (OMS2), denoted by the red curves.

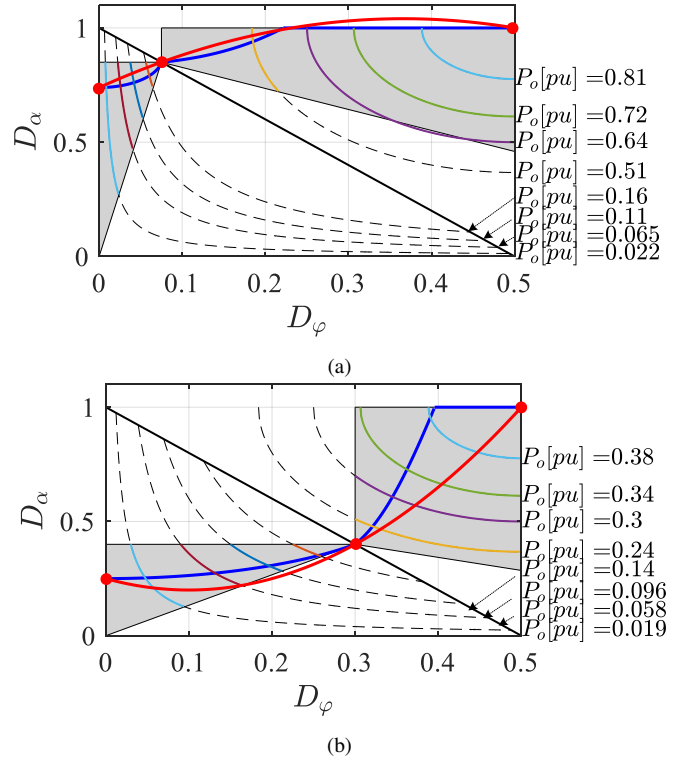


Fig. 12. Two ZVS failure cases for  $D_{\alpha,opt2}$  in boost scenarios (a)  $k = 0.85$  (b)  $k = 0.4$  in unified modulation scheme (OMS2)

on the varying voltage ratio  $k$ , the red curve could exceed the gray ZVS range. For example, two failed cases caused by too large or too small  $k$  in boost scenarios are shown in Fig. 12, where part of the red curve is beyond the ZVS region. Therefore, there is a limited range of  $k$  for unified modulation.

In order to satisfy  $D_{\alpha,opt2} \leq 1$  for any value of  $D_\varphi$  in  $[0, 0.5]$ , the symmetry axis of (23) should be larger than 0.5, then the maximum value of  $k$  can be solved, which is

$$\frac{(2k-1)(2-k)}{4(3k-2)} \geq \frac{1}{2} \rightarrow k_{max} = 0.78 \quad (25)$$

On the other hand, in order to avoid the situation shown in Fig. 12(b),  $D_{\alpha,opt2}$  in (23) should be larger than the ZVS border  $2kD_\varphi/(1-k)$  for any  $D_\varphi \in [0, (1-k)/2]$ , leading to

$$\frac{k^2}{2(3k^2-5k+2)} \geq \frac{1-k}{2} \rightarrow k_{min} = 0.45 \quad (26)$$

Similarly, the  $k$  range for (24) can be obtained in the same way, which is within  $[1.28, 2.23]$  in buck scenarios for unified modulation scheme.

2) *Partially Unified Modulation Scheme (OMS3)*: Seen from Table VI, EPS transfers into SPS ( $D_{\alpha,opt1} = 1$ ) in heavy load. If the SPS is kept for easy control, the complex optimal expressions in light and medium load can be unified with one expression. In this regard, another group of three points  $[0, k/(2-k)]$ ,  $[(1-k)/2, k]$  and  $[(k-1+\sqrt{1-k^2})/(2k), 1]$  in boost scenarios are used for curve fitting, and the  $D_\alpha$  is

kept at 1 in the range of  $D_\varphi \in [(k-1+\sqrt{1-k^2})/(2k), 0.5]$ . The simplified result will be

$$D_{\alpha,opt3} = \begin{cases} A_k \cdot D_\varphi^2 + B_k \cdot D_\varphi + C_k, & 0 < D_\varphi < \frac{k + \sqrt{1-k^2} - 1}{2k} \\ 1, & \frac{k + \sqrt{1-k^2} - 1}{2k} \leq D_\varphi \leq \frac{1}{2} \end{cases} \quad (27)$$

with

$$\begin{cases} A_k = \frac{(8-8k-4k^2)\sqrt{1-k^2} + 8k^3 - 8k^2 - 8k + 8}{k(2-k)(1-k^2)} \\ B_k = \frac{(4-4k-2k^2)\sqrt{1-k^2} + 2k^3 - 6k^2 - 4k + 4}{k(k+1)(k-2)} \\ C_k = \frac{k}{2-k} \end{cases} \quad (28)$$

Applying a similar change into the buck scenarios, the curve fitting results are as follows.

$$D_{\alpha,opt3} = \begin{cases} A_k \cdot D_\varphi^2 + B_k \cdot D_\varphi + C_k, & 0 < D_\varphi < \frac{1-k+\sqrt{k^2-1}}{2} \\ 1, & \frac{1-k+\sqrt{k^2-1}}{2} \leq D_\varphi \leq \frac{1}{2} \end{cases} \quad (29)$$

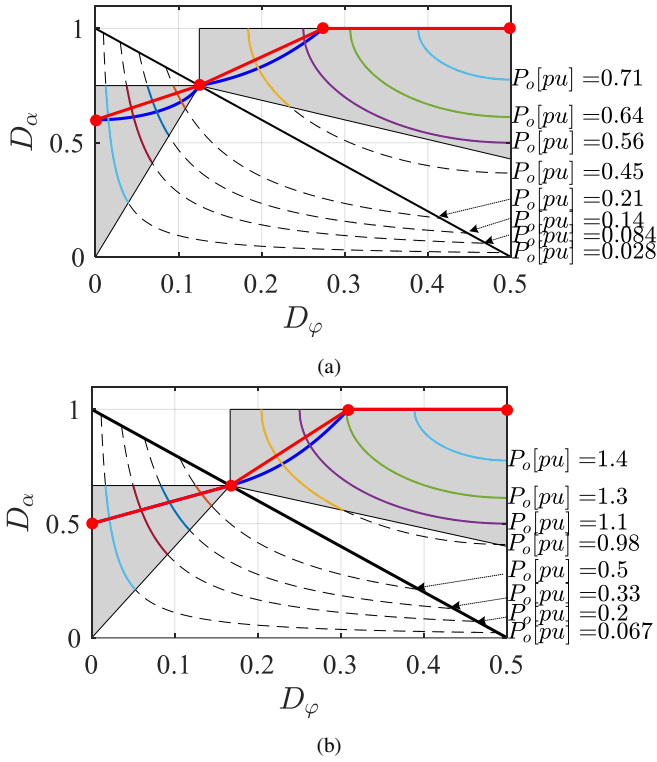


Fig. 13. The linearized relationship function of (a) (31) for Boost scenarios ( $k = 0.75$  in this case). (b) (32) for Buck scenarios ( $k = 1.5$  in this case) in linear modulation scheme (OMS4), denoted by the red curves.

with

$$\begin{cases} A_k = \frac{4k[(2k^2 - 2k - 1)\sqrt{k^2 - 1} + 2(k + 1)(k - 1)^2]}{2k^3 - k^2 - 2k + 1} \\ B_k = \frac{(4k + 2 - 4k^2)\sqrt{k^2 - 1} - 4k^3 + 4k^2 + 6k - 2}{2k^2 + k - 1} \\ C_k = \frac{1}{2k - 1} \end{cases} \quad (30)$$

Similar to the unified modulation scheme (OMS1), the voltage ratio in (27) and (29) needs to be limited within  $[0.56, 0.91]$  and  $[1.10, 1.80]$ , respectively.

3) *Linearized Modulation Scheme (OMS4)*: One common drawback of OMS2 and OMS3 is the limited range of voltage ratio  $k$ . In order to overcome this, a piecewise linear approximation scheme can be derived by considering the three load situations individually. Therefore, the four key points are all taken into account to linearize the complex expressions in Table VI, resulting in

$$D_{\alpha, opt4} = \begin{cases} \frac{2k}{2-k} D_{\varphi} + \frac{k}{2-k}, & D_{\varphi} \in [0, \frac{1-k}{2}] \\ \frac{(2-2k^2+2\sqrt{1-k^2})}{k(1+k)} D_{\varphi} - \frac{(1-k)\sqrt{1-k^2}+1-k-2k^2}{k(1+k)}, & D_{\varphi} \in [\frac{1-k}{2}, \frac{k-1+\sqrt{1-k^2}}{2k}] \\ 1, & D_{\varphi} \in [\frac{k-1+\sqrt{1-k^2}}{2k}, 0.5] \end{cases} \quad (31)$$

in boost scenarios and

$$D_{\alpha, opt4} = \begin{cases} \frac{2}{2k-1} D_{\varphi} + \frac{1}{2k-1}, & D_{\varphi} \in [0, \frac{k-1}{2k}] \\ \frac{2k\sqrt{k^2-1}+2k^2-2}{k+1} D_{\varphi} - \frac{(k-1)\sqrt{k^2-1}+k^2-k-2}{k+1}, & D_{\varphi} \in [\frac{k-1}{2k}, \frac{1-k+\sqrt{k^2-1}}{2}] \\ 1, & D_{\varphi} \in [\frac{1-k+\sqrt{k^2-1}}{2}, 0.5] \end{cases} \quad (32)$$

in buck scenarios.

Fig. 13 gives two cases derived from (31) and (32), respectively. It can be clearly seen that no matter how the voltage ratio changes, the linearized red curves will always locate within the gray ZVS area. Accordingly, the linearized modulation scheme (OMS4) is set free from the voltage ratio limitation.

### C. Comparison of Different Optimized Schemes

Based on different voltage ratio requirements and the preferred working conditions of the converter, the approximation principles of OMS2 ~ OMS4 have been explained in Section IV-B. Compared to the original OMS1 in Section IV, the three simplified schemes have their own pros and cons. In the following, a detailed comparison will be performed from different perspectives.

Firstly, with regard to the unification (depending on  $D_{\varphi}$ ), it can be evaluated by the number of segments in the relationship functions between  $D_{\alpha}$  and  $D_{\varphi}$ , which is represented by the stars number in the second column of Table VII. More segments means poorer unification performance. Although both OMS1 and OMS4 have the same three segments, the OMS4 is easier to implement due to the linear approximation.

Then the voltage ratio limitations (i.e.  $k$  range) are compared for different schemes. As shown in last section, OMS1 and OMS4 can theoretically guarantee ZVS for any value of  $k$ , whereas a limited range should be considered for OMS2 and OMS3 to avoid ZVS failure over the whole power transfer range. In this regard, OMS1, OMS4 are better than OMS2, OMS3.

From the point of calculation burden, two conditions of the voltage ratio are considered, i.e. a fixed or a varying  $k$ . If  $V_1$  and  $V_2$  are fixed, the voltage ratio can be seen as a constant and thereby the  $k$ -depending coefficients (e.g.  $A_k, B_k, C_k$ ) of  $D_{\alpha, opti}$  ( $i = 1, 2, 3, 4$ ) expressions are also constants. On this basis,  $D_{\alpha, opt4}$  has the simplest form due to the lower number of mathematical multiplications and square roots, which also means faster processing speed for the digital processor. This advantage will become further clear when multiple DAB modules are working at the same time. On the other hand, if  $V_1$  and  $V_2$  are varying, the sampling speed of  $V_1, V_2$  and the calculation burden of the  $k$ -depending coefficients should be taken into account. Regarding this, it can be found that OMS2 surpasses the other schemes, represented by four stars in Table VII.

At last, assuming the converter works in steady state, the input and output voltages are stabilized with a fixed  $k$ . In respect of this, the complexity of different schemes are evaluated by adding the star numbers from the second to fourth column in

TABLE VII  
COMPARISON OF OMS1, OMS2, OMS3 AND OMS4

|      | Unification | Voltage limitation | Calculation burden |             | Complexity |
|------|-------------|--------------------|--------------------|-------------|------------|
|      |             |                    | fixed $k$          | varying $k$ |            |
| OMS1 | ★           | ★★                 | ★                  | ★           | 4 · ★      |
| OMS2 | ★★★         | ★                  | ★★                 | ★★★★        | 6 · ★      |
| OMS3 | ★★          | ★                  | ★★★                | ★★          | 6 · ★      |
| OMS4 | ★           | ★★                 | ★★★★               | ★★★         | 7 · ★      |

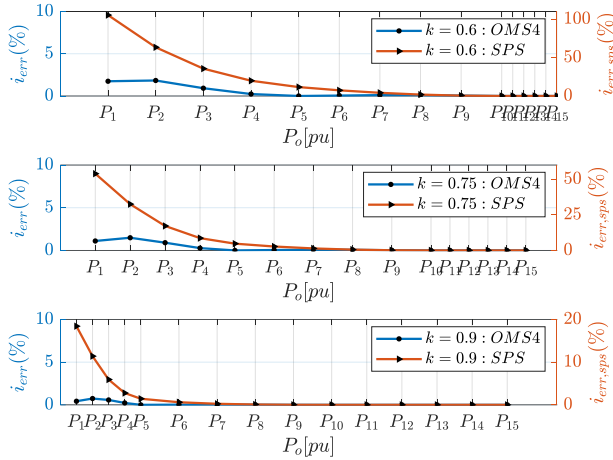


Fig. 14. Relative errors defined by (33) varying with voltage ratios and output powers

Table VII, and the summations are shown in the last column. It can be seen that OMS has the highest 7 stars, and thus will be selected as the focus to further evaluate the effectiveness on reducing conduction losses.

## V. RESULTS AND DISCUSSION

As illustrated in IV-C, the linearized modulation scheme (OMS4) overtakes other schemes with a simpler form of modulation expression. However, OMS4 is essentially an approximating method, and this means that the effectiveness on conduction losses reduction is not as good as OMS1 which can achieve minimum leakage inductance current  $I_{s,rms}$ . Hence the relative error calculated by (33) is used to measure the deviation from the minimum  $I_{s,rms}$ .

$$i_{err} = \frac{|I_{s,rms,OMS4} - I_{s,rms,OMS1}|}{I_{s,rms,OMS1}} \cdot 100\% \quad (33)$$

For comparison, the values of  $I_{s,rms}$  under SPS modulation is also calculated, and the following relative error between  $I_{s,rms,sp}$  and the minimum  $I_{s,rms,OMS1}$  is used to compare with (33).

$$i_{err,sp} = \frac{|I_{s,rms,sp} - I_{s,rms,OMS1}|}{I_{s,rms,OMS1}} \cdot 100\% \quad (34)$$

The calculated results varying with different voltage ratios and normalized output powers are shown in Fig. 14. Therein,

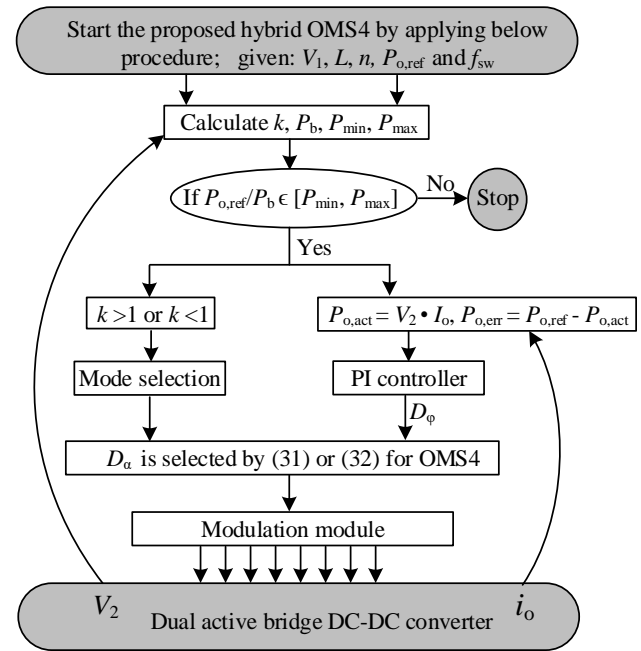


Fig. 15. Procedure of applying linearized modulation scheme (OMS4) to the DAB converter

$P_5$ ,  $P_{10}$  and  $P_{15}$  are the  $k$ -related output powers at the three boundary points (i.e.  $[(1-k)/2, k]$ ,  $[(k-1+\sqrt{1-k^2})/(2k), 1]$ ,  $[0.5, 1]$  that define the three segments in OMS4 in boost operation scenarios). Then the various other power levels  $P_i$  ( $i = 1..15$ ) can be expressed by

$$P_i = \begin{cases} 0.2 \cdot i \cdot P_5, & i = 1..5 \\ P_5 + 0.2 \cdot (i - 5) \cdot (P_{10} - P_5), & i = 6..10 \\ P_{10} + 0.2 \cdot (i - 10) \cdot (P_{15} - P_{10}), & i = 11..15 \end{cases} \quad (35)$$

with

$$P_5 = 2k^2(1 - k), P_{10} = \frac{2(k^2 - 1 + \sqrt{1 - k^2})}{k}, P_{15} = k \quad (36)$$

From Fig. 14, it can be seen that  $i_{err,sp}$  is larger than  $i_{err,OMS4}$ , especially in light load and medium load. When the voltage ratio  $k$  is 0.6, the maximum  $i_{err,sp}$  even exceeds 100%. Consequently, it can be obtained that OMS4 is more applicable to the DAB converter, especially when the converter works in light load and the voltage ratio deviates far from unity. On the other hand, comparing  $I_{s,rms,OMS4}$  with the optimal  $I_{s,rms,OMS1}$ , the relative errors  $i_{err}$  are very small (less than 2%) for various voltage ratios and output power levels, especially in medium and high power load ( $P_5 \sim P_{15}$ , less than 0.5%), which proves the effectiveness of linearized modulation scheme on reducing the conduction losses. The process of applying OMS4 to the DAB converter is illustrated in Fig. 15.

An experimental platform for the DAB converter is built to validate the linearized modulation scheme OMS4, as shown in Fig. 16. The main circuit parameters are listed in Table VIII.

In order to fully evaluate the performance improvement caused by linearized modulation scheme, two groups of com-

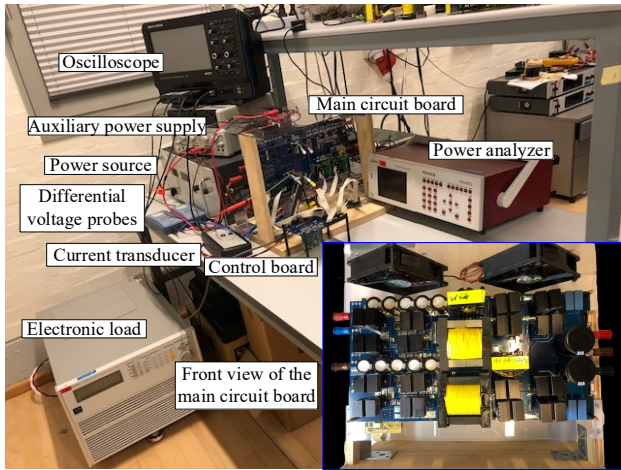


Fig. 16. Test platform for the DAB converter

TABLE VIII  
SYSTEM SPECIFICATIONS

| Parameters | Description                       | Value        |
|------------|-----------------------------------|--------------|
| $P$        | Rating power                      | 1.5 kW       |
| $n : 1$    | Turns ratio of the transformer    | 3.5 : 1      |
| $f_{sw}$   | Switching frequency               | 60 kHz       |
| $T_{dead}$ | Dead time                         | 400 ns       |
| $L_s$      | Series inductor                   | 36.2 $\mu$ H |
| $L_{trp}$  | Primary-side leakage inductance   | 4.5 $\mu$ H  |
| $L_{trs}$  | Secondary-side leakage inductance | 372.5 nH     |
| $C_1$      | Primary DC capacitor              | 0.78 mF      |
| $C_2$      | Secondary DC capacitor            | 1.5 mF       |

parative experiments are conducted for each mode: group one (G1) adopts the optimized linear modulation (OMS4) and the other group (G2) does not use any optimized scheme (but still modulated by EPS). Moreover, for the purpose of highlighting the effect of the conduction losses, the operating points of two groups are both located within the ZVS range. As shown in IV-B3, the piecewise linear scheme has three segments. Therefore, for either boost or buck scenarios, the measured working waveforms with three different output power levels are shown in the following.

In Mode I, the steady state waveforms of the DAB converter are illustrated in Fig. 17, where  $v_p$  and  $v_s$  are voltage waveforms generated by HB<sub>1</sub> and HB<sub>2</sub>, and  $i_p$ ,  $i_s$  are the primary and secondary transformer current, respectively. Fig. 17(a) shows the measured waveforms when the DAB converter works without adopting any optimized modulation (belongs to G2). Fig. 17(b) shows the working waveforms when the converter is modulated by linearized scheme (belongs to G1). The output power for both situations is given at 190 W. As marked in the figure, the value of  $I_{s,rms}$  in Fig. 17(b) is lower than that in Fig. 17(a), indicating the effectiveness of OMS4 in reducing the conduction losses of the DAB converter. As a result, the overall system efficiency is improved from 92.5% to 95%. Besides, in order to directly see if the ZVS is achieved, the drain-source voltage and the gate signal of  $S_7$  (turned on at the rising edge of  $v_s$ ) are illustrated in Fig. 17(c) and Fig.

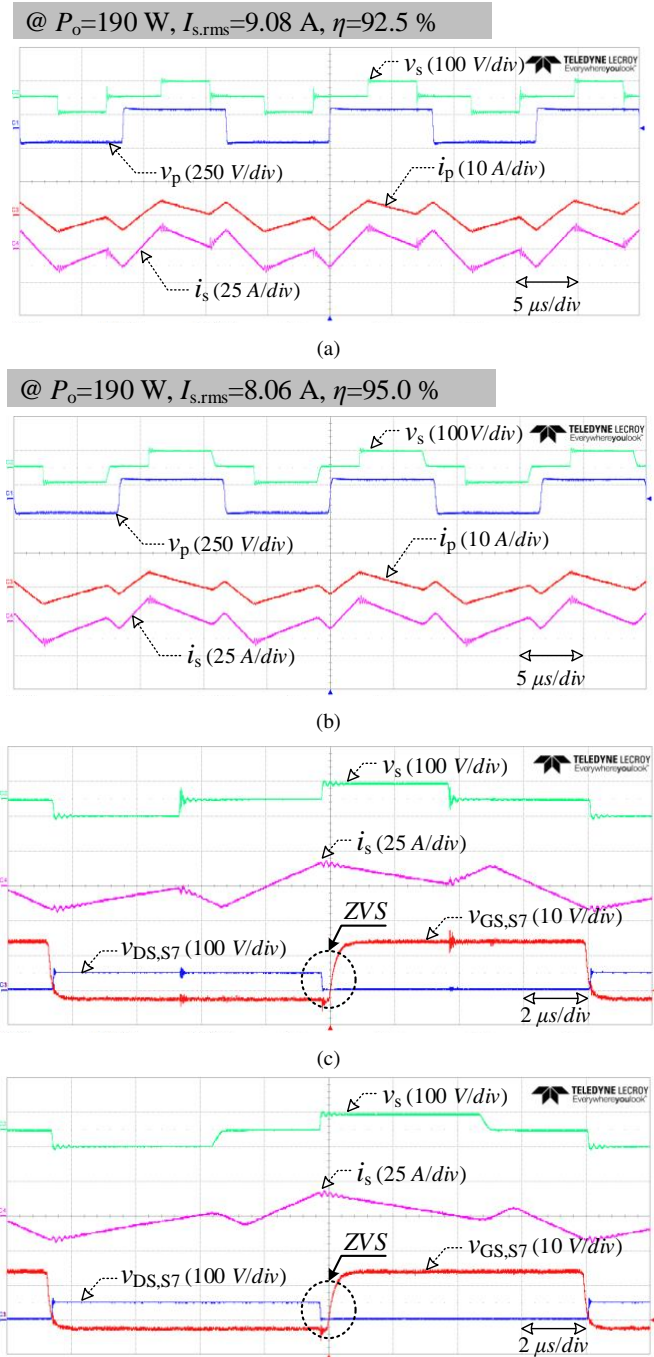


Fig. 17. Experimental waveforms of DAB converter in Mode I where  $V_1=120$  V,  $V_2=46$  V ( $k = 0.75$ ) (a) working waveforms without optimized modulation (b) working waveforms with linearized modulation scheme (c) ZVS realization without optimized modulation (d) ZVS realization with linearized modulation scheme.

17(d), corresponding to the working conditions in Fig. 17(a) and Fig. 17(b), respectively. It can be seen that the switching-on signal (i.e. rising edge) of  $v_{GS,S7}$  comes after the drain-source voltage  $v_{DS,S7}$  becoming zero, which implies that the transistor  $S_7$  has achieved zero-voltage turn-on.

In Mode II, the converter is operated at two power levels (i.e. 430 W and 700 W) and the working waveforms are shown in Fig. 18 and Fig. 19, respectively. Although there

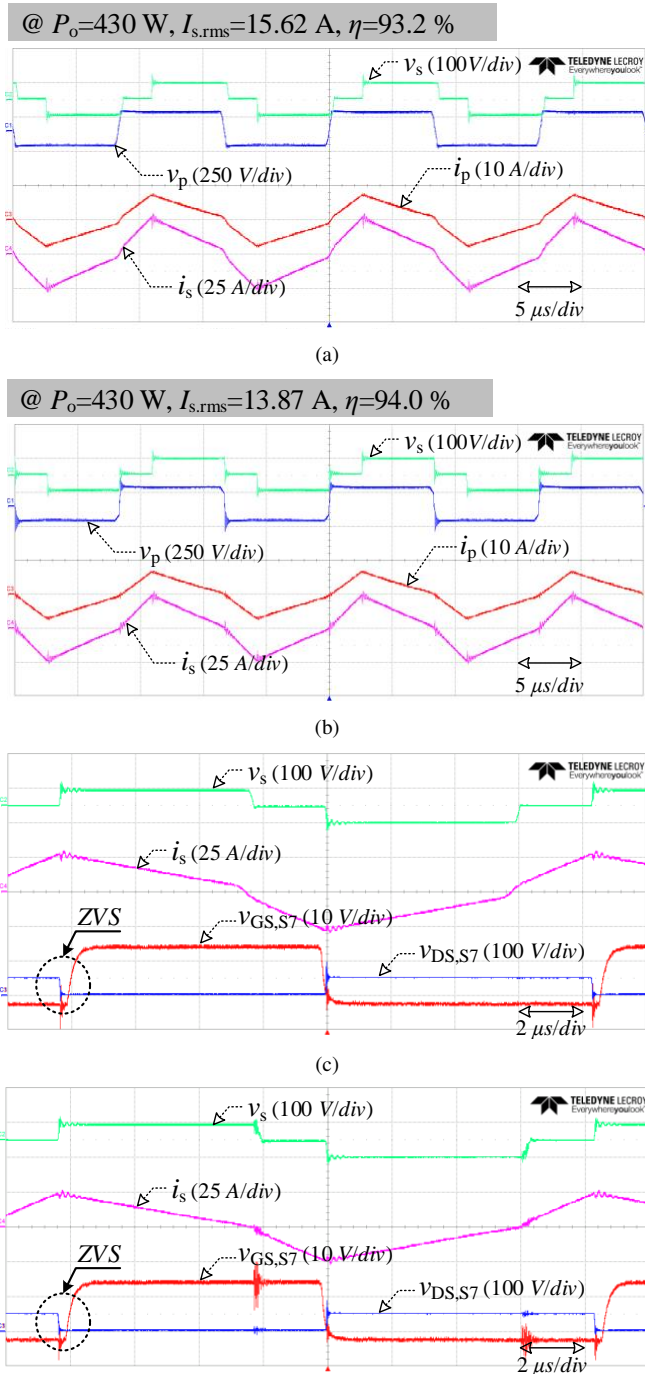


Fig. 18. Experimental waveforms of DAB converter in Mode II where  $V_1=120$  V,  $V_2=46$  V ( $k = 0.75$ ) (a) working waveforms without optimized modulation (b) working waveforms with linearized modulation scheme (c) ZVS realization without optimized modulation (d) ZVS realization with linearized modulation scheme.

are some oscillations at the switching-on instants of  $S_7$ , the voltage across  $S_7$  is kept at zero when the gate signal reaches high level, thus ZVS is still guaranteed in these two higher power situations. On the other hand, compared to Fig. 18(a) and Fig. 19(a), the converter efficiency is improved when the optimized linear modulation scheme is utilized in Fig. 18(b) and Fig. 19(b), respectively.

In terms of buck scenarios, Fig. 20 ~ Fig. 22 present

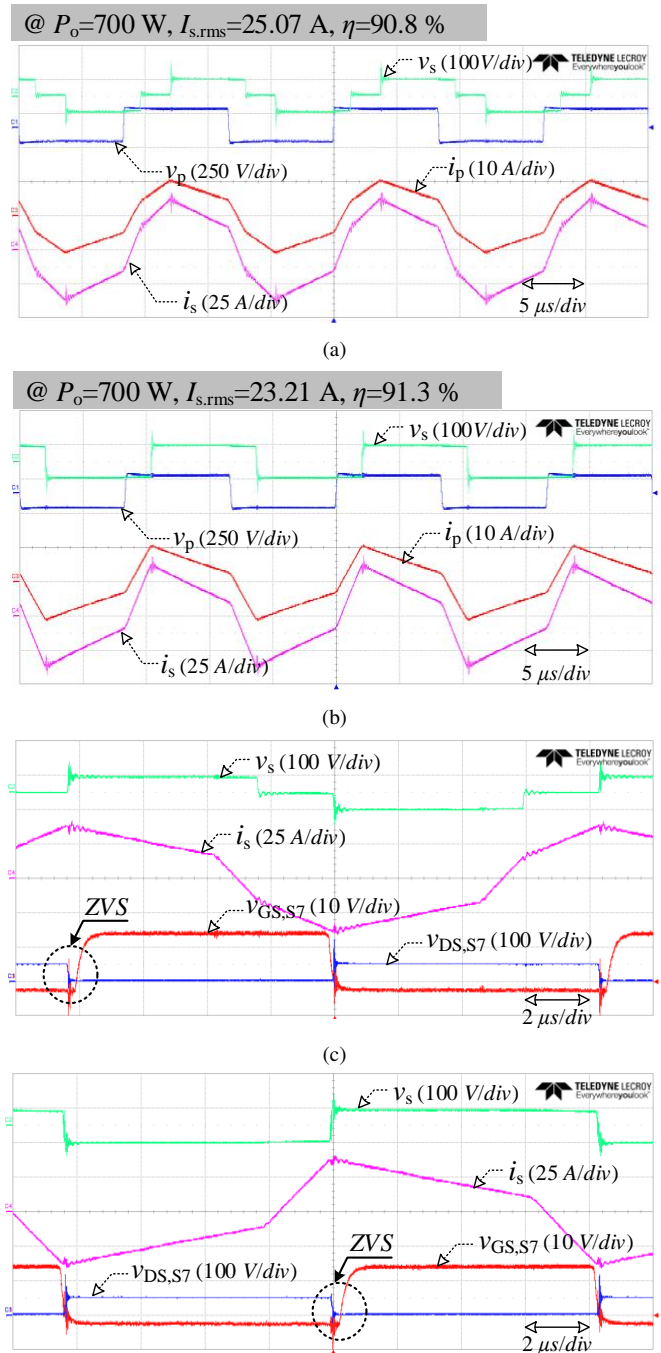


Fig. 19. Experimental waveforms of DAB converter in Mode II where  $V_1=120$  V,  $V_2=46$  V ( $k = 0.75$ ) (a) working waveforms without optimized modulation (b) working waveforms with linearized modulation scheme (c) ZVS realization without optimized modulation (d) ZVS realization with linearized modulation scheme.

the corresponding waveforms for Mode III and Mode IV, respectively. Similar conclusions can be achieved with reduced conduction losses and improved efficiency. Also, the ZVS is realized at different output power levels.

Besides, the linear OMS4 is essentially a hybrid modulation scheme, consisting of EPS in light, medium load and SPS in heavy load. This can be seen from the expressions (31) and (32) and the working waveforms in Fig. 19 and Fig. 22. By switching the converter between light load and heavy load with

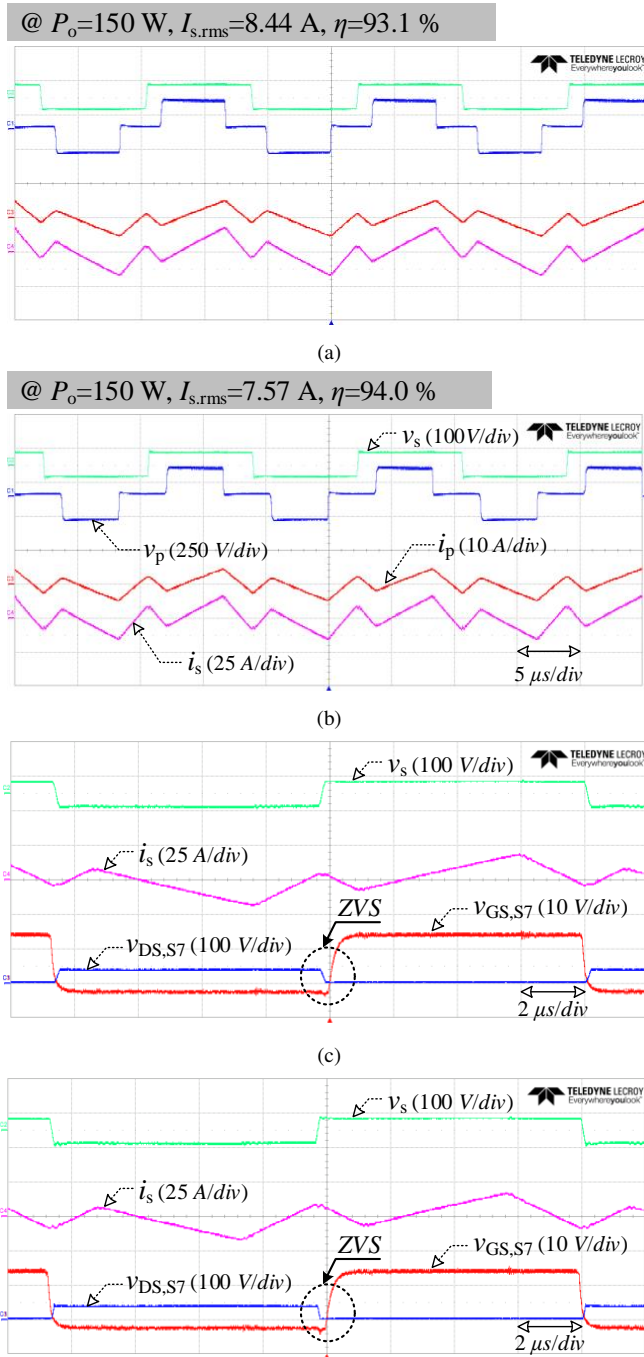


Fig. 20. Experimental waveforms of DAB converter in Mode III where  $V_1=190$  V,  $V_2=36$  V ( $k = 1.5$ ) (a) working waveforms without optimized modulation (b) working waveforms with linearized modulation scheme (c) ZVS realization without optimized modulation (d) ZVS realization with linearized modulation scheme.

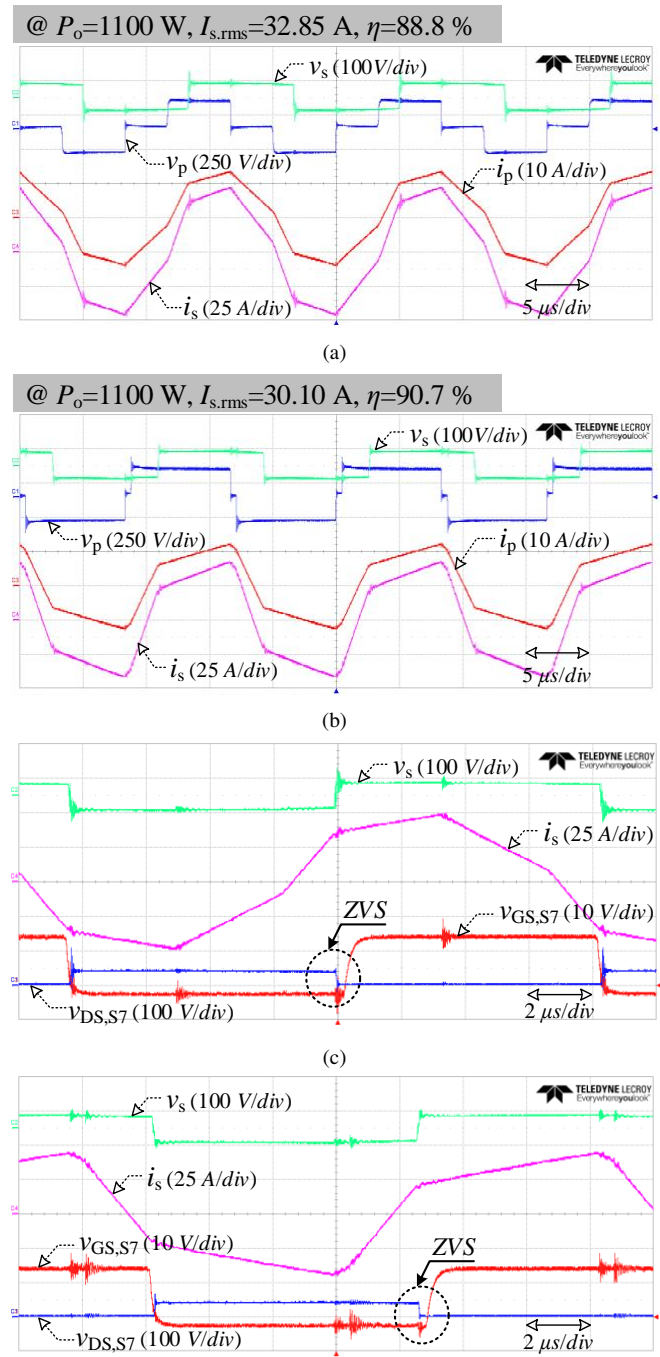


Fig. 21. Experimental waveforms of DAB converter in Mode IV where  $V_1=190$  V,  $V_2=36$  V ( $k = 1.5$ ) (a) working waveforms without optimized modulation (b) working waveforms with linearized modulation scheme (c) ZVS realization without optimized modulation (d) ZVS realization with linearized modulation scheme.

OMS4, the dynamic response is shown in Fig. 23, where  $V_2$  is the output dc voltage,  $i_o$  is the output current and  $i_s$  is the leakage inductance current referred to the secondary side. The power is increased from 150 W to 700 W in Fig. 23(a) and then decreased in Fig. 23(b). Part of  $i_s$  is amplified in green frames for having a clear view on the current shape of  $i_s$ . It can be seen that the converter can smoothly changes from EPS to SPS or reverse depending on the power condition.

Furthermore, the input and output voltage are changed to

operate the converter with different voltage ratios, and the measured efficiency curves are shown in Fig. 24. Corresponding to boost and buck scenarios, Fig. 24(a) ( $k = 0.9$ ) and Fig. 24(b) ( $k = 1.2$ ) plot the converter efficiency at different output powers. In the figure, three situations are illustrated: the red curve denotes the linearized modulation scheme (belongs to G1), the blue curve represents the normal EPS modulation without any optimization (belongs to G2) and the black curve

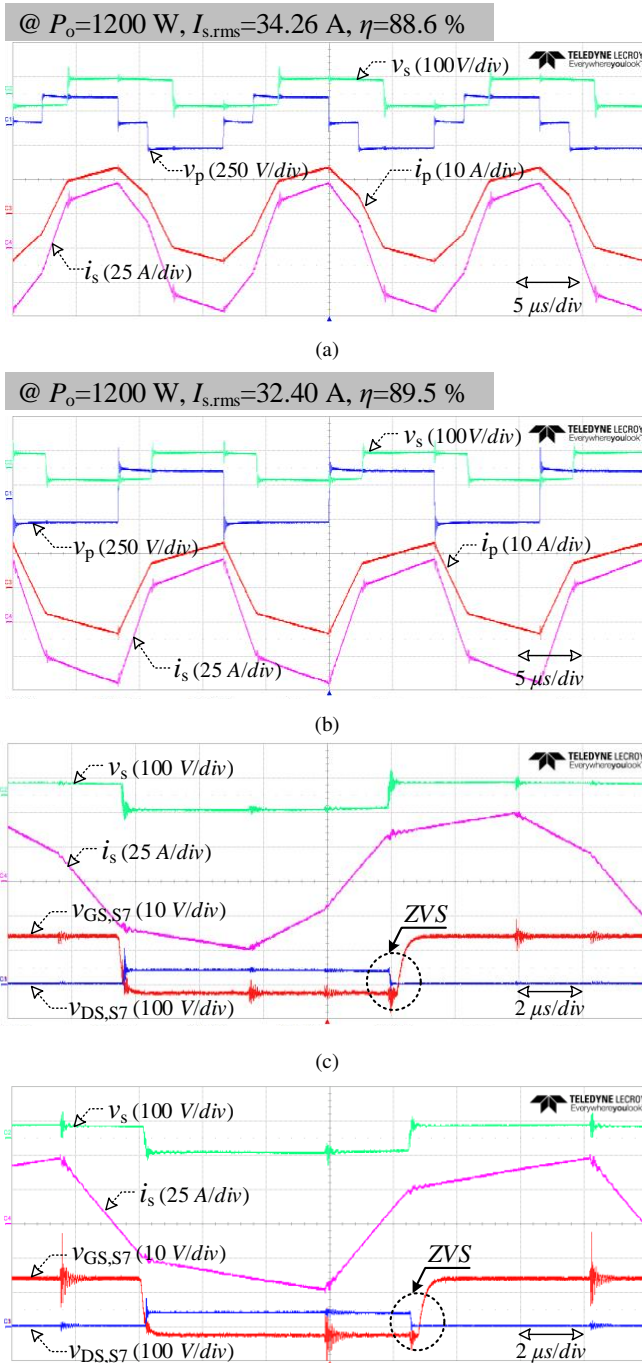


Fig. 22. Experimental waveforms of DAB converter in Mode III where  $V_1=190$  V,  $V_2=36$  V ( $k = 1.5$ ) (a) working waveforms without optimized modulation (b) working waveforms with linearized modulation scheme (c) ZVS realization without optimized modulation (d) ZVS realization with linearized modulation scheme.

is the resulted efficiency by applying SPS over the whole power range. Among the three situations, the linearized modulation scheme has a better efficiency performance in either boost or buck scenarios. In light load, due to the ZVS failure in SPS (black curve), the induced switching losses result in lower efficiency compared to the other two situations (G1 and G2). When the converter works with higher output power, the linearized modulation transfer into SPS scheme and thus the

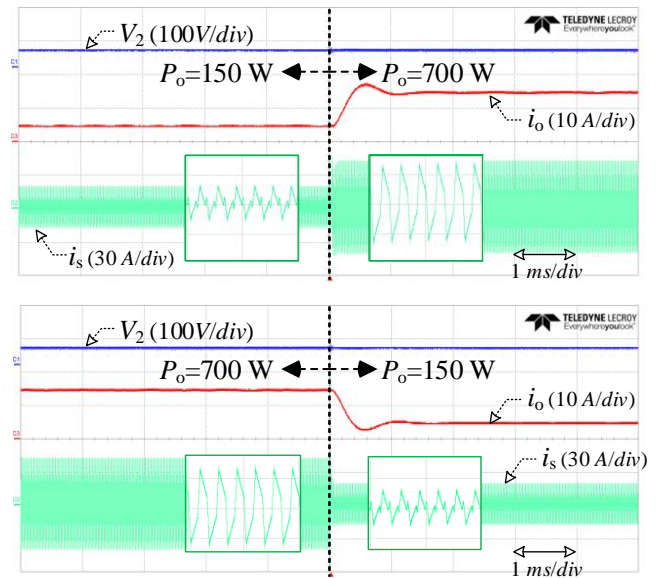


Fig. 23. Dynamic response with the output power (a) increased from 150 W to 700 W (b) decreased from 700 W to 150 W in boost scenario ( $V_1=120$  V,  $V_2=46$  V).

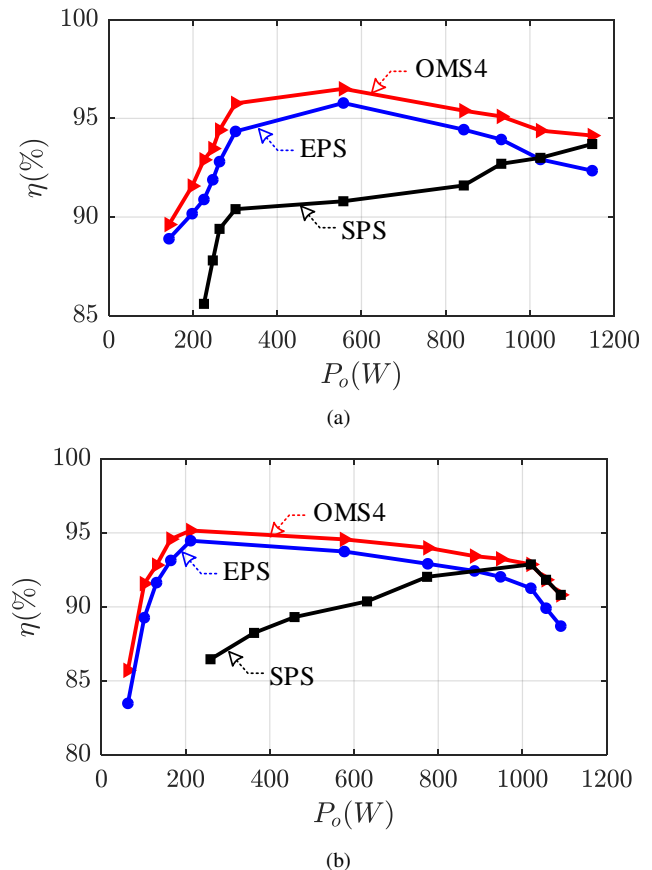


Fig. 24. Measured efficiency curves of the DAB converter for different output power levels, where the red curve, blue curve and black curve denote the converter efficiencies with linear modulation scheme (G1), without any optimization (G2) and with SPS, respectively. (a) Boost operation,  $V_1=190$  V,  $V_2=60$  V ( $k = 0.9$ ) (b) Buck operation,  $V_1=190$  V,  $V_2=45$  V ( $k = 1.2$ ).

red curve and the black curve are overlapped in heavy load

conditions. In terms of G2 (blue curve), since it can also achieve ZVS, the efficiency is higher than SPS in light and medium load, but lower than G1 because of the larger leakage inductance current.

## VI. CONCLUSIONS

In order to reduce the conduction losses of the DAB converter and still keep other performance parameters unchanged, an optimized hybrid modulation scheme is proposed in this paper. On the basis of achieving ZVS over the whole operation range and maintaining the same power transfer ability as the single phase shift modulation, an optimal modulation scheme is firstly derived with minimum leakage inductance current. By exploring the possibility to further simplify the relationship functions between the control variables, three other modulation schemes are presented considering various voltage ratio requirements and working conditions for the DAB converter. Therein, the linearized modulation scheme is prominent with less complexity after a through comparative analysis and thus is selected as the focus of this paper. By operating the converter with linear modulation scheme, the conduction losses can be effectively reduced and the system efficiency is improved. Comparative experiments are implemented to highlight the conduction losses reduction and in addition, the experimental results also validate the ZVS realization with linear modulation.

## REFERENCES

- [1] R. D. Doncker, D. Divan, and M. Kheraluwala, "A three-phase soft-switched high power density DC/DC converter for high power applications," in *Conference Record of the 1988 IEEE Industry Applications Society Annual Meeting*, IEEE, 1988.
- [2] N. M. L. Tan, T. Abe, and H. Akagi, "Design and performance of a bidirectional isolated DC-DC converter for a battery energy storage system," *IEEE Trans. Power Electron.*, vol. 27, no. 3, pp. 1237–1248, 2012.
- [3] S. Inoue and H. Akagi, "A bidirectional DC-DC converter for an energy storage system with galvanic isolation," *IEEE Trans. Power Electron.*, vol. 22, no. 6, pp. 2299–2306, 2007.
- [4] X. Wang, F. Tian, and I. Batarseh, "High efficiency parallel post regulator for wide range input DC-dc converter," *IEEE Trans. Power Electron.*, vol. 23, no. 2, pp. 852–858, Mar. 2008.
- [5] J. Biela, U. Badstuebner, and J. W. Kolar, "Impact of power density maximization on efficiency of DC-dc converter systems," *IEEE Trans. Power Electron.*, vol. 24, no. 1, pp. 288–300, Jan. 2009.
- [6] N. M. L. Tan, N. M. L. Tan, S. Inoue, S. Inoue, A. Kobayashi, and H. Akagi, "Voltage balancing of a 320-V, 12-F electric double-layer capacitor bank combined with a 10-kW bidirectional isolated DC-DC converter," *IEEE Trans. Power Electron.*, vol. 23, no. 6, pp. 2755–2765, Nov. 2008.
- [7] M. B. Camara, H. Gualous, F. Gustin, A. Berthon, and B. Dakyo, "DC/dc converter design for supercapacitor and battery power management in hybrid vehicle applications—polynomial control strategy," *IEEE Trans. Ind. Electron.*, vol. 57, no. 2, pp. 587–597, Feb. 2010.
- [8] F. Z. Peng, and J. S. Lawler, "A new ZVS bidirectional DC-dc converter for fuel cell and battery application," *IEEE Trans. Power Electron.*, vol. 19, no. 1, pp. 54–65, Jan. 2004.
- [9] R. T. Naayagi, A. J. Forsyth, and R. Shuttleworth, "High-power bidirectional DC-dc converter for aerospace applications," *IEEE Trans. Power Electron.*, vol. 27, no. 11, pp. 4366–4379, Nov. 2012.
- [10] Z. Wang, B. Liu, L. Guan, Y. Zhang, M. Cheng, B. Zhang, and L. Xu, "A dual-channel magnetically integrated EV chargers based on double-stator-winding permanent-magnet synchronous machines," *IEEE Trans. Ind. Appl.*, vol. 55, no. 2, pp. 1941–1953, Mar. 2019.
- [11] Z. Wang, B. Liu, Y. Zhang, M. Cheng, K. Chu, and L. Xu, "The chaotic-based control of three-port isolated bidirectional dc/dc converters for electric and hybrid vehicles," *Energies*, vol. 9, no. 2, p. 83, 2016.

- [12] H. Bai and C. Mi, "Eliminate reactive power and increase system efficiency of isolated bidirectional dual-active-bridge DC-dc converters using novel dual-phase-shift control," *IEEE Trans. Power Electron.*, vol. 23, no. 6, pp. 2905–2914, Nov. 2008.
- [13] H. Wu, Y. Lu, T. Mu, and Y. Xing, "A family of soft-switching DC-dc converters based on a phase-shift-controlled active boost rectifier," *IEEE Trans. Power Electron.*, vol. 30, no. 2, pp. 657–667, Feb. 2015.
- [14] G. Xu, D. Sha, Y. Xu, and X. Liao, "Hybrid-bridge-based DAB converter with voltage match control for wide voltage conversion gain application," *IEEE Trans. Power Electron.*, vol. 33, no. 2, pp. 1378–1388, Feb. 2018.
- [15] B. Zhao, Q. Yu, and W. Sun, "Extended-phase-shift control of isolated bidirectional DC-dc converter for power distribution in microgrid," *IEEE Trans. Power Electron.*, vol. 27, no. 11, pp. 4667–4680, Nov. 2012.
- [16] F. Li, Y. Li, and X. You, "Optimal dual-phase-shift control strategy of an isolated buck-boost converter with a clamped inductor," *IEEE Trans. Power Electron.*, vol. 33, no. 6, pp. 5374–5385, Jun. 2018.
- [17] B. Liu, P. Davari, and F. Blaabjerg, "A flexible control scheme for single-stage DAB AC/DC converters," in *Proc. IEEE Int. Power Electronics and Application Conf. and Exposition (PEAC)*, Nov. 2018, pp. 1–6.
- [18] X. Liu, Z. Q. Zhu, D. A. Stone, M. P. Foster, W. Q. Chu, I. Urquhart, and J. Greenough, "Novel dual-phase-shift control with bidirectional inner phase shifts for a dual-active-bridge converter having low surge current and stable power control," *IEEE Trans. Power Electron.*, vol. 32, no. 5, pp. 4095–4106, May 2017.
- [19] G. Xu, D. Sha, J. Zhang, and X. Liao, "Unified boundary trapezoidal modulation control utilizing fixed duty cycle compensation and magnetizing current design for dual active bridge DC-dc converter," *IEEE Trans. Power Electron.*, vol. 32, no. 3, pp. 2243–2252, Mar. 2017.
- [20] B. Liu, P. Davari, and F. Blaabjerg, "An optimized control scheme to reduce the backflow power and peak current in dual active bridge converters," in *2019 IEEE Applied Power Electronics Conference and Exposition (APEC)*, IEEE, 2019, pp. 1622–1628.
- [21] C. Calderon, A. Barrado, A. Rodriguez, P. Alou, A. Lazaro, C. Fernandez, and P. Zumel, "General analysis of switching modes in a dual active bridge with triple phase shift modulation," *Energies*, vol. 11, no. 9, p. 2419, 2018.
- [22] O. M. Hebala, A. A. Aboushady, K. H. Ahmed, and I. Abdelsalam, "Generic closed-loop controller for power regulation in dual active bridge DC-dc converter with current stress minimization," *IEEE Trans. Ind. Electron.*, vol. 66, no. 6, pp. 4468–4478, Jun. 2019.
- [23] B. Zhao, Q. Song, W. Liu, and W. Sun, "Current-stress-optimized switching strategy of isolated bidirectional DC-dc converter with dual-phase-shift control," *IEEE Transactions on Industrial Electronics*, vol. 60, no. 10, pp. 4458–4467, Oct. 2013.
- [24] J. Huang, Y. Wang, Z. Li, and W. Lei, "Unified triple-phase-shift control to minimize current stress and achieve full soft-switching of isolated bidirectional DC-dc converter," *IEEE Transactions on Industrial Electronics*, vol. 63, no. 7, pp. 4169–4179, Jul. 2016.
- [25] N. Hou, W. Song, and M. Wu, "Minimum-current-stress scheme of dual active bridge DC-dc converter with unified phase-shift control," *IEEE Transactions on Power Electronics*, vol. 31, no. 12, pp. 8552–8561, Dec. 2016.
- [26] Q. Gu, L. Yuan, J. Nie, J. Sun, and Z. Zhao, "Current stress minimization of dual-active-bridge DC-dc converter within the whole operating range," *IEEE Journal of Emerging and Selected Topics in Power Electronics*, vol. 7, no. 1, pp. 129–142, Mar. 2019.
- [27] H. Shi, H. Wen, J. Chen, Y. Hu, L. Jiang, G. Chen, and J. Ma, "Minimum-backflow-power scheme of DAB-based solid-state transformer with extended-phase-shift control," *IEEE Trans. Ind. Appl.*, vol. 54, no. 4, pp. 3483–3496, Jul. 2018.
- [28] H. Wen, W. Xiao, and B. Su, "Nonactive power loss minimization in a bidirectional isolated DC-dc converter for distributed power systems," *IEEE Trans. Ind. Electron.*, vol. 61, no. 12, pp. 6822–6831, Dec. 2014.
- [29] A. Tong, L. Hang, G. Li, X. Jiang, and S. Gao, "Modeling and analysis of a dual-active-bridge-isolated bidirectional DC/dc converter to minimize RMS current with whole operating range," *IEEE Trans. Power Electron.*, vol. 33, no. 6, pp. 5302–5316, Jun. 2018.
- [30] S. Chakraborty and S. Chattopadhyay, "Minimum-RMS-current operation of asymmetric dual active half-bridge converters with and without ZVS," *IEEE Trans. Power Electron.*, vol. 32, no. 7, pp. 5132–5145, Jul. 2017.
- [31] W. Choi, K. Rho, and B. Cho, "Fundamental duty modulation of dual-active-bridge converter for wide-range operation," *IEEE Trans. Power Electron.*, vol. 31, no. 6, pp. 4048–4064, Jun. 2016.

- [32] G. G. Oggier and M. Ordonez, "High-efficiency DAB converter using switching sequences and burst mode," *IEEE Trans. Power Electron.*, vol. 31, no. 3, pp. 2069–2082, Mar. 2016.
- [33] F. Krismer and J. W. Kolar, "Closed form solution for minimum conduction loss modulation of DAB converters," *IEEE Trans. Power Electron.*, vol. 27, no. 1, pp. 174–188, Jan. 2012.
- [34] H. Zhou and A. M. Khambadkone, "Hybrid modulation for dual-active-bridge bidirectional converter with extended power range for ultracapacitor application," *IEEE Trans. Ind. Appl.*, vol. 45, no. 4, pp. 1434–1442, Jul. 2009.
- [35] J. Everts, F. Krismer, J. Van den Keybus, J. Driesen, and J. W. Kolar, "Optimal ZVS modulation of single-phase single-stage bidirectional DAB AC–dc converters," *IEEE Trans. Power Electron.*, vol. 29, no. 8, pp. 3954–3970, Aug. 2014.
- [36] J. Hiltunen, V. Väisänen, R. Juntunen, and P. Silventoinen, "Variable-frequency phase shift modulation of a dual active bridge converter," *IEEE Trans. Power Electron.*, vol. 30, no. 12, pp. 7138–7148, Dec. 2015.
- [37] H. Akagi, T. Yamagishi, N. M. L. Tan, S. Kinouchi, Y. Miyazaki, and M. Koyama, "Power-loss breakdown of a 750-V 100-kW 20-kHz bidirectional isolated DC–dc converter using SiC-MOSFET/sbd dual modules," *IEEE Trans. Ind. Appl.*, vol. 51, no. 1, pp. 420–428, Jan. 2015.
- [38] T. Cappello, A. Santarelli, and C. Florian, "Dynamic ron characterization technique for the evaluation of thermal and off-state voltage stress of GaN switches," *IEEE Trans. Power Electron.*, vol. 33, no. 4, pp. 3386–3398, Apr. 2018.
- [39] W. A. Roshen, "A practical, accurate and very general core loss model for nonsinusoidal waveforms," *IEEE Transactions on Power Electronics*, vol. 22, no. 1, pp. 30–40, Jan. 2007.
- [40] M. P. D. Graovac and A. Kiep, "Mosfet power losses calculation using the datasheet parameters," Available online at <https://www.infineon.com>, Tech. Rep., 2008.
- [41] B. Liu, P. Davari, and F. Blaabjerg, "An optimized control scheme for reducing conduction and switching losses in dual active bridge converters," in *Proc. IEEE Energy Conversion Congress and Exposition (ECCE)*, Sep. 2018, pp. 622–629.